

Dynamical structure factors of dynamical quantum simulators

M. L. Baez,^{1,2,*} M. Goihl,² J. Haferkamp,² J. Bermejo-Vega,³ M. Gluza,² and J. Eisert^{2,4}

¹Max Planck Institute for the Physics of Complex Systems, Dresden, Germany

²Dahlem Center for Complex Quantum Systems, Freie Universität Berlin, Germany

³University of Granada, Av. Fuentenueva s/n. 18071, Granada, Spain

⁴Helmholtz-Zentrum Berlin für Materialien und Energie, Germany

(Dated: July 19, 2022)

The dynamical structure factor is one of the experimental quantities crucial in scrutinizing the validity of the microscopic description of strongly correlated systems. However, despite its long-standing importance, it is exceedingly difficult in generic cases to numerically calculate it, ensuring that the necessary approximations involved yield a correct result. Acknowledging this practical difficulty, we discuss in what way results on the hardness of classically tracking time evolution under local Hamiltonians are precisely inherited by dynamical structure factors; and hence offer in the same way the potential computational capabilities that dynamical quantum simulators do: We argue that practically accessible variants of the dynamical structure factors are BQP-hard for general local Hamiltonians. Complementing these conceptual insights, we improve upon a novel, readily available, measurement setup allowing for the determination of the dynamical structure factor in different architectures, including arrays of ultra-cold atoms, trapped ions, Rydberg atoms, and superconducting qubits. Our results suggest that quantum simulations employing near-term noisy intermediate scale quantum devices should allow for the observation of features of dynamical structure factors of correlated quantum matter in the presence of experimental imperfections, for larger system sizes than what is achievable by classical simulation.

I. INTRODUCTION

The field of condensed matter physics has seen a lot of successes since its origin. On one hand, analytical tools and the concept of integrability allows us to use several toy models to study different natural phenomena to a great deal of success, as in the case of spin systems or superconducting behaviour [1–8]. On the other hand, with the advent of powerful computational tools, the field kept advancing, now being able to study more complex, non-integrable systems, closer to realistic materials. For the last several decades, classical algorithms such as Monte Carlo techniques [9], exact diagonalization [10], tensor networks [11] and more, have offered some of the greatest insights into the most surprising behaviour of many different systems. However, the field of computational condensed matter physics has been confronted with the same problem time and time again: the more we understand, the more complex the models we wish to study become. And while the current numerical techniques are still extremely useful, in many cases the system sizes need to be constrained to a couple dozen atomic sites to obtain an efficient simulation, or the algorithms are just efficient for a narrow class of models. The fundamental reason this crisis is manifesting arises from the fact that each one of these physical problems can be connected to a computational problem which belong to a (in many cases) well determined complexity class [12]. The computational complexity of these problems tells us how efficiently a given problem can be solved with a given resource, bounding the possible performance of any algorithm using that resource. Despite the field slowly pushing the boundaries of what is possible with recent new methodology in the form of tensor network methods, AI algorithms, and others, the complexity

boundary cannot be surpassed with classical algorithms. As long as the resource is a classical simulation, and considering certain assumptions believed to be true in the field of complexity theory [13, 14], we know how far we can go. For example, in higher dimensional frustrated quantum magnets or high- T_c superconductors, we have no generic efficient way of calculating some of the most important time dependent quantum expectation values needed to understand the properties of the particular phase of interest. In particular, the extent to which these systems can be simulated classically is limited. Quantum Monte Carlo is a powerful method that however is affected by strong sign problems for frustrated and fermionic systems, and there are severe complexity-theoretic obstacles to the extent to which the sign problem can be cured [15, 16] or eased [17]. Exact diagonalization can yield a plethora of useful results for many different physical systems, but the computational resources required scale exponentially in the system size, allowing one to only solve systems with a handful of lattice sites in the generic case. Other more sophisticated methods such as MPS, PEPS, MERA, etc. are efficient for one dimensional short-range systems, but these methods are constrained by the amount of entanglement present in the system, rendering an efficient simulation of higher dimensional, long-ranged, systems and excited states a challenging task.

In this work, we propose dynamical analogue quantum simulators [18, 19] as an alternative method to simulate low energy excitations of strongly correlated matter. In particular we suggest that *dynamical structure factors*, which provide key physical insights into quantum matter, can be accessed with quantum simulators, while at the same time is a quantity which is significantly less accessible with classical computers.

Large scale analogue quantum simulation platforms are unique systems in that they show exceptionally strong quantum effects and allow for measuring expectation values of microscopic observables [20–27]. These simulators create synthetic systems featuring the same physical behaviour we

* Corresponding author: baez@pks.mpg.de

want to understand. Among other platforms, ultra-cold atoms trapped in optical lattices offer a promising direction towards building large scale quantum simulators yielding physical insights of practical importance. Propagation of excitations in XXZ models [20, 21], Lieb-Robinson bounds [22], relaxation dynamics [28], and phase diagrams of Fermi-Hubbard models [23] are just a few of the exciting phenomena which can be probed with ultra-cold atoms beyond capabilities of current classical algorithms. At the same time, quantum simulations with trapped ions and Rydberg arrays have also seen several breakthroughs. As for example, the quantum dynamics of the long range transverse field Ising model, which have recently been studied in systems of over fifty atoms via time dependent expectation values of single spin observables [24–27]. Furthermore, many-body localization effects have been probed in all these setups, as well as on superconducting qubits [29, 30]. Each one of these setups have specific advantages. On the one hand, optical lattices allow for large system sizes and low-energy many-body states. On the other hand, trapped ions experiments have an excellent stability and a very broad range of observables, as well as tomographic methods with which to study them, while Rydberg arrays, built through atom-by-atom assembly, allow for a large versatility of lattice geometries [31] and physical effects [32]. Though a great body of observations has been assembled, a particular question arises: *Can quantum simulators provide qualitative dynamical quantities of systems relevant in the condensed matter context, for which there is evidence that in the regime discussed they are inaccessible to classical algorithms?*

We propose an answer to this question in form of the *dynamical structure factor (DSF)*, a widely attainable experimental observable which gives information regarding the dynamical properties of a given system. In materials it is experimentally measured by inelastic neutron scattering [33] and resonant inelastic X-ray scattering [34]. Given the relative ease of measuring the DSF experimentally, an efficient way to simulate this quantity for the different theoretical models which aim at explaining the phenomena of those systems becomes imperative. We argue that the DSF can be accurately accessed with quantum simulators within the experimental level of accuracy currently available in the different architectures, and for system sizes beyond what current classical algorithms can achieve, as we show in Fig. 1.

The DSF is a quantity which can be considered stable to small perturbations of the microscopic model whose excitations it probes, given that the qualitative features of the DSF already provide a lot of information regarding those excitations. In this sense, we expect to see an inherent robustness in the DSF, finding that observing excitation gaps and continua is possible with state of the art setups in the presence of moderate experimental imperfections. As a proof of principle we investigate the short and long range transverse field Ising model (TFIM). In this context we point out that the DSF can indeed be seen to be robust to realistic experimental imperfections. Since the short range model is integrable [39], it allows us to study relatively big system sizes comparable to those achievable in trapped ions and Rydberg atoms simulators. Furthermore, the behaviour of the long range model,

Simulation of time dependent two body observables in long range models

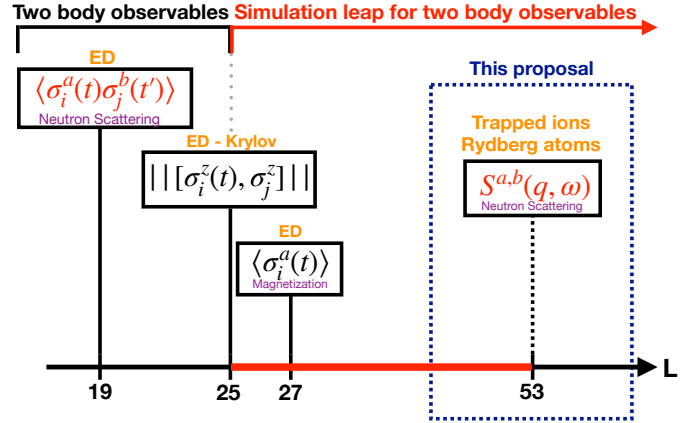


Figure 1. *State of the art exact numerical algorithms to time evolve two body observables for the long range TFIM.* We show the larger system sizes which can access unequal time correlators (and by extension DSFs). In orange we show the methods that have been employed, or are proposed, to calculate the different quantities. In purple, we show the experimental techniques that are used to measure those same quantities in material experiments. At 19 sites, the Pauli operators at different sites have been time evolved via exact diagonalization (ED) to obtain unequal time correlators at zero temperature [35]. Using Krylov space methods, the system size has been extended to 25 sites to study out of time ordered correlators at infinite temperature [36]. System sizes up to 27 (ED) and 128 (Lanczos and t-DRMG) sites have been obtained, but only single site observables have been accessed [37]. Here we show that our proposal offers a leap forward in terms of the system sizes that can be employed to study DSFs of long range models via quantum simulation. Please note that using variational methods, entanglement entropies up to 125 sites can be obtained [38].

for a given range of parameter values, approaches that of the short range model. As such, we first study in detail the effects of experimental imperfections in the short range model, to give us an intuition of those effects. We observe that the Fourier transform involved in the calculation of the DSF acts as a noise filter, rendering the effects of the imperfections to be well controlled for the current levels of experimental accuracy. Once the short range model is well understood, we move to our application proposal for a quantum advantage in a related system which is hard to numerically simulate, namely the measurement of the DSF for the long range transverse field Ising model.

The numerical calculation of unequal time correlation functions in long range systems is constrained to system sizes much smaller than what current quantum simulators can achieve (on the order of fifty sites for trapped ions and Rydberg atoms [24, 25], to a couple hundred sites for optical lattices). Thus, we propose *the measurement of the DSF for the long range transverse field Ising model as a practical application of quantum simulators in a quantity relevant for both condensed matter and material science.*

Since both the short and long range models can be understood in terms of a two kink picture [35], we study the long

range transverse field Ising model under the same imperfections as for the short range model. We show that the experimental imperfections currently present in quantum simulators, do not affect the DSF in a significant way, and that the effect on the DSF is qualitatively the same as for the short range model. Furthermore, we show that the scaling of the errors in the DSF is well controlled in the full range of system sizes studied here, indicating that the scaling of the quantum simulation to sizes larger than what state of the art numerical algorithms can achieve is expected to be well controlled.

We also study the computational hardness of evaluating the DSF for general systems. We find that the DSF can be likened to a BQP-hard problem, meaning that any classical algorithm calculating it for general Hamiltonians efficiently would also efficiently solve all the tasks that a quantum computer can tackle efficiently. The latter is regarded in the quantum computing community as a highly unlikely scenario. As such, realizing our proposal in practice would tackle a task hard for classical computers in a field of practical importance in condensed matter physics. While the specific proposal of this work is centred on a specific model which has already been implemented, it is worth pointing out that the proof of hardness is valid for a wide range of Hamiltonians, indicating that the possibility of quantum advantage goes beyond the transverse field Ising model. It is our aim in this work to highlight a specific case in which the DSF can be experimentally achieved in the near term, but the protocol employed here, together with the error analysis and the study of the different architectures can be easily applied to other models, as for example the XY model in superconducting chips [29] or Rydberg atoms [40]. As such, future advances in the field, where analogue quantum simulators implement further models in higher dimensions can make use of the study performed in this work to show a practical application of quantum simulators through the DSF in those models.

This work is organized as follows: In Section II, we describe the measurement protocol, and its tomography based extension, and how these protocols can be employed to obtain the DSF of a given model using quantum simulators. In Section III we prove that calculating both, the DSF for finite time intervals as well as unequal time correlators, is BQP-hard and that the errors arising from time discretization are bounded. We follow in Section IV with a brief description of what is known about the physics of our two test cases, namely the short- and long-range TFIM. After this, in Section V, we describe how we quantify the effect of experimental imperfections and study the effect of them on the DSF of the short range TFIM. Finally in Section VI, we show how the long range TFIM is affected by experimental imperfections and show via finite size scaling that the errors on the DSF are controlled and small when the system size is scaled up.

II. DSF IN QUANTUM SIMULATORS

As we have mentioned in the introduction, several quantum architectures can access a number of physical models with interesting behaviours, relevant for both the quantum many

body dynamics, and the condensed matter community. While in all these architectures improvements are continuously reported, the measurement of unequal time observables and DSFs in particular, which allow for the direct study of low energy excitations, has still not been achieved.

Taking into consideration the current experimental capabilities, it is natural to study the possibility of obtaining a DSF in a quantum simulator where the Hamiltonian implemented is that of a spin chain. While different Hamiltonians as the XXZ [20], Ising [26], and XY [40] have already been implemented in these setups, in this work we will concentrate on the short and long range transverse field Ising models, since these systems have already been implemented and studied in the past in the context of quantum simulation.

In order to employ quantum simulators to study the DSF of solid state systems, we want to probe the fluctuations of their ground states or thermal states via *unequal time correlation functions*. For a spin system with lattice sites $i, j \in \Lambda$ (where Λ is the collection of lattice sites), these are defined by

$$C_{i,j}^{a,b}(t) = \langle \sigma_i^a(0) \sigma_j^b(t) \rangle, \quad (1)$$

we denote Pauli matrices by σ^a with $a = x, y, z$. One should notice that the spin operator at lattice site j is evolved forwards to time t in the Heisenberg picture, while the other is not. The Fourier transform of these quantities from real-space sites \mathbf{x}_i to momentum $\mathbf{q} \in \mathbb{R}^3$ and time- to frequency-domain $\omega \in \mathbb{R}$ yields the DSF

$$S^{a,b}(\mathbf{q}, \omega) = \frac{1}{N} \sum_{i,j \in \Lambda} \int_{-\infty}^{\infty} dt e^{-i\mathbf{q} \cdot (\mathbf{x}_i - \mathbf{x}_j)} e^{i\omega t} C_{i,j}^{a,b}(t), \quad (2)$$

where N is the number of lattice sites. There has been a recent proposal [41] on how to measure retarded Green's functions (which are related to the DSF in equilibrium via the fluctuation-dissipation theorem) in cold atoms and trapped ion devices using *Ramsey spectroscopy*, however a clear understanding of the feasibility of observing important physical effects and the DSF itself, when the proposal of Ref. [41] is applied to a quantum many-body system is still lacking.

In Fig. 2 we show a typical DSF for the transverse field Ising model, one of the models we will study in detail in this work, away from criticality. In the figure we observe a cosine shaped continuum, with a gap at $q = 0$. The goal of this work is to show that a DSF like the one in Fig. 2 can be obtained from state of the art quantum simulations. In Section IV we will describe in detail the particularities of this DSF, as well as the physical interpretation of the continuum and the gap in terms of low energy excitations of the transverse field Ising model.

To obtain DSFs as the one in Fig. 2 in quantum simulators, the crucial ingredient that needs to be supplemented beyond the existing techniques is a measurement protocol which gives access to unequal time correlation functions as in Eq. (1). In the following, we propose a generalization of the protocol proposed by [41], which can be employed in any setup where a single site spin rotation can be implemented. We extend this spectroscopy protocol via tomographic methods to systems which do not exhibit as many symmetries as Ref. [41]

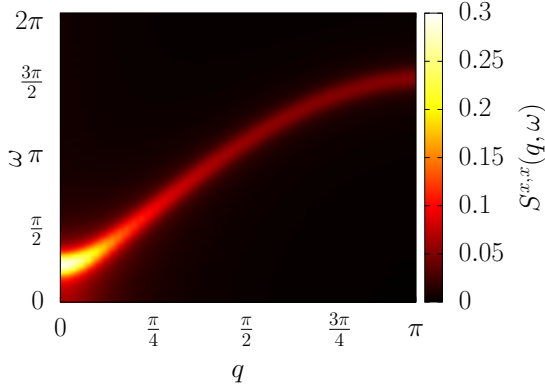


Figure 2. *Dynamical structure factor for the transverse field Ising model.* We show the DSF away from the criticality, $J = 1$ and $B = 1.4$, according to Eqs. (28) and (30). We observe the gap around the $q = 0, \omega = \pi/4$ point, and the ω -dependent two particle continuum extending over the entire reciprocal space, in accordance with the exact solution of the transverse field Ising model [39].

assumes. In this context, we offer a measurement protocol which can be implemented in many different architectures, as trapped ions, Rydberg atoms, and super-conducting qubit chips, and for a wide class of systems beyond Ising and XXZ as has previously been proposed [41]. Thus we are opening the door to the simulation of the DSF of several different models and to the cross verification of these DSFs between different experimental platforms.

A. DSF measurement protocol

The DSF effectively probes low energy excitations of a given system, described by a particular Hamiltonian H . Given the definition of the DSF in Eq. (2), the excitations to which it is sensitive are those related to observables of the form given in Eq. (1). The first step to obtain such a quantity then resides in the *initialization* of the quantum simulator in a low energy state, ideally the ground state of H . In this section we will assume, for the sake of simplicity, that the quantum simulator will be initialized in the unique ground state vector of H , which we refer to as $|\psi_0\rangle$, though in principle, the protocol we employ can be used with any initial state be it in equilibrium or not, as exemplified in Ref. [42] with the Ramsey spectroscopy technique.

Preparing such state can be achieved by adiabatic evolution. At the same time, the recently proposed *quantum approximate optimization algorithms* (QAOAs) can also been employed. These algorithms have recently been reported in trapped ions experiments [43], achieving a very good approximation of the ground state of non-trivial Hamiltonians. It is worth pointing out that QAOAs have been shown to considerably reduce the experimental time required for ground state preparation in comparison to adiabatic evolutions in trapped ions, effectively extending the evolution times which can be achieved with this particular architecture.

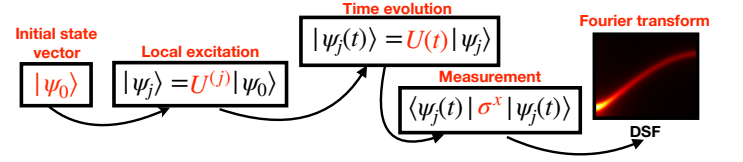


Figure 3. *General scheme for measuring the DSF in quantum simulators:* 1) Prepare the initial state vector, which in this work is the ground state. 2) Excite it locally via a unitary single spin rotation at site j , $U^{(j)}$. 3) Evolve this state with the Hamiltonian H to see how the local energy surplus is redistributed through elementary excitations, $U(t)$. 4) Finally, measure a local spin observable at a site different than j , which in our case is the local magnetization $\langle \sigma^x \rangle$. Processing such data via Fourier transforms allows us to obtain the DSF.

Once the ground state is obtained, we then induce low energy excitations by applying a single *spin rotation*. After exciting the system locally, the state is *evolved* with the Hamiltonian H . Finally, after the evolution, we *measure* local spin operators with single-site resolution. We can see a general sketch of this measurement protocol in Fig. 3. Once the unequal time correlators are measured, the DSF can be obtained via a spatial and temporal Fourier transform.

B. Measuring unequal time correlations

Let us now discuss the crucial question at hand: How can we measure two point *unequal time* correlation functions if we can only perform unitary transformations and measure local spin operators? If observables in the Heisenberg picture would be evolved to an equal time, we would naturally get access to equal time correlation functions such as $\langle \sigma_i^a(t) \sigma_j^b(t) \rangle$, but in our case the desired correlations are time displaced of the form $\langle \sigma_i^a(0) \sigma_j^b(t) \rangle$ as defined in Eq. (1). The main insight of Ref. [41] (see also Ref. [42] for a detailed study of the idea) has been that the operator at initial time $\sigma_i^a(0)$ can be obtained as part of a unitary operation, the pulse of *Ramsey interferometry*.

We begin by the basic, and at the same time most important, example of this idea: Consider the unitary representing a $\frac{\pi}{4}$ -rotation of a spin at site $j \in \Lambda$ along of the x -axis

$$U^{(j)} = \frac{1}{\sqrt{2}}(1 - i\sigma_j^x). \quad (3)$$

We would like to use it as an *excitation* of a low-energy state vector $|\psi_0\rangle$ which then is probed by subsequent evolution $U(t)$ to time t governed by the many-body Hamiltonian of the interacting system being investigated. To keep the discussion simple let us assume that the expectation value of an odd number of spin operators vanishes for $|\psi_0\rangle$ (as is the case for the TFIM and arises from the symmetries of the Hamiltonian and initial state [41]). We show in the next section how this assumption can be relaxed by a tomographic analysis.

Having these two ingredients at hand, we can consider the

state vector

$$|\psi\rangle = U(t)U^{(j)}|\psi_0\rangle \quad (4)$$

which can be obtained by an appropriate *unitary* single-qubit rotation $U^{(j)}$ that locally excites the system (as the one in Eq. (3)) and a subsequent time evolution of the system $U(t)$. Observe that both operations are unitary and thus $|\psi\rangle$ is a state vector. If we measure the expectation value of σ_i^x on this state we obtain

$$\begin{aligned} \langle\psi|\sigma_i^x|\psi\rangle &= \frac{1}{2}\langle\psi_0|(\mathbb{1} + i\sigma_j^x)\sigma_i^x(t)(\mathbb{1} - i\sigma_j^x)|\psi_0\rangle \\ &= \frac{1}{2}\langle\psi_0|\sigma_i^x(t)|\psi_0\rangle - \frac{i}{2}\langle\psi_0|\sigma_i^x(t)\sigma_j^x|\psi_0\rangle \\ &\quad + \frac{i}{2}\langle\psi_0|\sigma_j^x\sigma_i^x(t)|\psi_0\rangle + \frac{1}{2}\langle\psi_0|\sigma_j^x\sigma_i^x(t)\sigma_j^x|\psi_0\rangle. \end{aligned} \quad (5)$$

The middle two terms of Eq. (5) are the *retarded Green function* $G_{x,x}^{\text{ret}}(i,j,t)$ given by

$$G_{x,x}^{\text{ret}}(i,j,t) = -\frac{i}{2}\langle\sigma_i^x(t)\sigma_j^x(0) - \sigma_j^x(0)\sigma_i^x(t)\rangle_0. \quad (6)$$

The first term in the last line of Eq. (5) can be measured directly by simply omitting the excitation step and hence can be subtracted from the data if it is non-zero. The last term, on the other hand, has a non-trivial unequal time dependence and hence must either vanish due to, e.g., symmetry arguments or has to be reconstructed.

The case considered in Ref. [41] is the one in which the Hamiltonian \hat{H} has a unitary symmetry \mathcal{P} , $\hat{H} = \mathcal{P}\hat{H}\mathcal{P}^\dagger$, with two basic properties. First, it leaves invariant the probed state vector $\mathcal{P}|\psi_0\rangle = |\psi_0\rangle$. And second, σ_j^x is odd, i.e., $\sigma_j^x = -\mathcal{P}\sigma_j^x\mathcal{P}$. Using the invariance of the Hamiltonian we find that this property is preserved in time $\sigma_j^x(t) = -\mathcal{P}\sigma_j^x(t)\mathcal{P}$. From these it follows that the last term above

$$R(i,j,t) = \langle\psi_0|\sigma_j^x\sigma_i^x(t)\sigma_j^x|\psi_0\rangle \quad (7)$$

must vanish. This is directly verified by inserting the identity $\mathbb{1} = \mathcal{P}\mathcal{P}^\dagger$, as

$$\begin{aligned} R(i,j,t) &= \langle\psi_0|\mathcal{P}(\mathcal{P}^\dagger\sigma_j^x\mathcal{P})(\mathcal{P}^\dagger\sigma_i^x(t)\mathcal{P})(\mathcal{P}^\dagger\sigma_j^x\mathcal{P})(\mathcal{P}^\dagger|\psi_0)\rangle \\ &= -\langle\psi_0|\sigma_j^x\sigma_i^x(t)\sigma_j^x|\psi_0\rangle = -R(i,j,t) = 0. \end{aligned} \quad (8)$$

We conclude that whenever a symmetry of this kind is present (as in e.g the TFIM where $\mathcal{P} = \prod_{j \in \Lambda} \sigma_j^z$) we obtain

$$\langle\psi|\sigma_i^x|\psi\rangle = \langle\psi_0|U^{(j)\dagger}\sigma_i^x(t)U^{(j)}|\psi_0\rangle = G_{x,x}^{\text{ret}}(i,j,t). \quad (9)$$

Calculating this for all spin pairs (i,j) we obtain the retarded Green function $G_{x,x}^{\text{ret}}(i,j,t)$ and we can perform a Fourier transform in real space and time to obtain $G_{x,x}^{\text{ret}}(\mathbf{q},\omega)$. Finally, we can relate the retarded Green function, when linear response theory holds, to the dynamical structure factor via the fluctuation-dissipation theorem

$$S^{xx}(\mathbf{q},\omega) = -\frac{1}{\pi}[1 + n_B(\omega)]\text{Im}[G_{x,x}^{\text{ret}}(\mathbf{q},\omega)], \quad (10)$$

where $n_B(\omega) = 1/(e^{\omega/T} + 1)$. In the case of $T \rightarrow 0$ we obtain

$$S^{xx}(\mathbf{q},\omega) = -\frac{1}{\pi}\text{Im}[G_{x,x}^{\text{ret}}(\mathbf{q},\omega)]. \quad (11)$$

This way, we get direct access to the dynamical structure factor by measuring the retarded Green's function via the above measurement protocol.

There are two points which need to be made before we move on: First, while we study the zero temperature DSF, finite but small temperatures will broaden the features of the DSF but not change the overall behaviour, provided that T is smaller than the smallest coupling of the model. Second, note that the fluctuation-dissipation theorem holds when linear response theory is a good approximation, and its validity or lack of thereof away from equilibrium is a highly researched topic to the date [19, 44, 45]. As such, this measurement protocol for the DSF will be accurate when the system is close to thermal equilibrium in a practical sense, indicating that a study of non equilibrium effects is, so far, only possible in the context of quantum simulation via the retarded Green function, and not via the DSF, as it has originally been proposed in Ref. [42].

C. Tomographic recovery methods for unequal time correlation functions

Here we will describe a tomographic approach to measuring expectation values of unequal time correlation functions in a way that does not require of the symmetry arguments employed above. If the symmetry argument can be relaxed, we can show how the term $R(i,j,t)$ can be extracted. Let us define a modified Ramsey state vector which reads

$$|\psi_\phi\rangle = U(t)U^{(j)}(\phi)|\psi_0\rangle \quad (12)$$

where now we excite the ground state $|\psi_0\rangle$ with a ϕ -rotation around the x -axis

$$\begin{aligned} U^{(j)}(\phi) &= e^{-i\phi\sigma_j^x} = \cos(\phi)\mathbb{1} - i\sin(\phi)\sigma_j^x \\ &=: c_\phi\mathbb{1} - is_\phi\sigma_j^x. \end{aligned} \quad (13)$$

For an analogous measurement to the case in the previous section we obtain

$$\begin{aligned} \langle\psi_\phi|\sigma_i^x|\psi_\phi\rangle &= c_\phi^2\langle\psi_0|\sigma_i^x(t)|\psi_0\rangle + 2c_\phi s_\phi G_{x,x}^{\text{ret}}(t) \\ &\quad + s_\phi^2 R(i,j,t). \end{aligned} \quad (14)$$

We now notice that we can directly measure the left hand side and the first term on last line of the expression above. For a fixed angle ϕ we can write

$$b_\phi = \langle\psi_\phi|\sigma_i^x|\psi_\phi\rangle - c_\phi^2\langle\psi_0|\sigma_i^x(t)|\psi_0\rangle. \quad (15)$$

Now, we can rewrite Eq. (14) as

$$a_\phi^T v = b_\phi \quad (16)$$

where v is the vector we want to reconstruct, given by

$$v = [G_{x,x}^{\text{ret}}(t), R(i,j,t)]^T \quad (17)$$

and $a_\phi = [2s_\phi c_\phi, s_\phi^2]$. If an experiment measures b_ϕ using various angles ϕ then we can build a matrix A using the different a_ϕ 's as rows and in a corresponding fashion we can collect the measured b_ϕ 's into a vector b .

The retarded Green's function can be reconstructed by noticing that

$$v^\star = (A^T A)^{-1} A^T b \quad (18)$$

gives the value of v that minimizes the least-square residue

$$\min_v \|Av - b\|_2. \quad (19)$$

Here we assume that one can choose the excitation angles ϕ in such a way that the matrix $A^T A$ is well conditioned as is done in typical tomographic schemes. In order to measure the DSF this procedure must be performed for all pairs of excitation and measurement positions $i, j \in \Lambda$ and the Fourier transform of the collection of reconstructed values $v_1^\star = G_{x,x}^{\text{ret}}(i, j, t)$ will yield the DSF. The second value of the reconstructed vector $v_2^\star = R(i, j, t)$ can be discarded for calculating the DSF, but it could also be interesting to quantify how a Hamiltonian not respecting the symmetry \mathcal{P} introduces deviations in the observables, or if a symmetric Hamiltonian can restore the symmetry, dynamically, if the initial state was not symmetric.

III. ON THE COMPUTATIONAL COMPLEXITY OF THE DSF

Once we have formalized how dynamical quantum simulators can access the DSF, we will concentrate on answering the question *how computationally hard is the calculation of the DSF?* In the following we formalize the statements about classical hardness and show that a practically accessible variant of the dynamical structure factor is hard for the complexity class BQP. In complexity theory, BQP stands for *bounded error quantum polynomial time* and it corresponds to the class of problems that can be solved by a quantum computer in a time which scales polynomial with system size, and with a bounded error probability. This signifies that it is intractable to efficiently compute the dynamical structure factor of general local Hamiltonians with a classical computer. To this end, we show that the building blocks of the DSF, the unequal time correlators $C_{i,j}^{a,b}(t)$ are BQP-hard to compute.

This section is different in style as it uses the language of computational complexity theory. Its purpose is to provide evidence that practical difficulties simulating dynamical structure factors in general are not due to a lack of imagination when it comes to efficient classical algorithms. The remainder of this work, however, can be understood independently of this section and an eager reader might skip it.

To start, and without loss of generality, we show that $\langle \sigma_i^z(t) \sigma_j^z \rangle_\psi := \langle \psi | \sigma_i^z(t) \sigma_j^z | \psi \rangle$ is BQP-hard to compute for product states $|\psi\rangle$ and for ground states. Then we use these observations to consider the DSF over a finite (but arbitrarily

large) interval of time

$$S_{t_0, t_1}^{z,z}(q, \omega) = \frac{1}{N} \sum_{i,j} \int_{t_0}^{t_1} e^{-iq(x_i - x_j)} e^{i\omega t} \langle \sigma_i^z(t) \sigma_j^z \rangle_\psi dt. \quad (20)$$

where N is the system size. In particular, we prove the following.

Theorem 1 (Hardness of computing the approximate dynamical structure factor). *For $t_1 - t_0 = \text{poly}(N)$, product states $|\psi\rangle$, and 2-local Hamiltonians it is BQP-hard to approximate $S_{t_0, t_1}^{z,z}(q, \omega)$ within an error $\varepsilon = \text{poly}'^{-1}(N)$.*

We consider the quantity $S_{t_0, t_1}^{z,z}$ instead of the full Fourier transform as it is the practically accessible one: Any time observation will necessarily be finite in practice. What is more, from a conceptual perspective, the latter is not even computable on a Turing machine due to arbitrarily large errors that are introduced by the Fourier transform: The continuous Fourier transform is not Turing computable [46].

A. Hardness for estimating correlators on ground states

For hardness of ground states, we observe that computing $C_{i,j}^{z,z}(t) = \langle \sigma_i^z(t) \sigma_j^z \rangle_\psi$ for any t is at least as hard as computing $C_{i,j}^{z,z}(0) = \langle \sigma_i^z \sigma_j^z \rangle_\psi$. First, computing correlators up to constant additive errors on ground states of quasi-local Hamiltonians is BQP-hard by the Feynman-Kitaev construction [47]. Furthermore this remains true for several classes of local observables and local Hamiltonians, including one-local observables measured on ground states of nearest-neighbour two-local Hamiltonians on qubits [48, 49], and two-local observables measured on ground states of translation invariant nearest-neighbour two-local Hamiltonians with local dimension three [50].

B. Hardness for out-of-time correlators

For the product states, we start with a general observation: Consider an arbitrary circuit $C_n = U_n \dots U_1$ consisting of k -local gates U_i . Evaluating the quantity $\langle \sigma_i^z(t) \sigma_j^z \rangle_\psi$ for product state vectors $|\psi\rangle$ within constant error is BQP-hard. Here, $0 \leq t \leq n$ is an integer. For $\text{Pr}(1)$, the probability of measuring 1, we obtain:

$$\begin{aligned} \text{Pr}(1) &= \langle \psi | C_t^\dagger \left(\frac{1 + \sigma_i^z}{2} \right) C_t | \psi \rangle \\ &= \frac{1}{2} \pm \frac{1}{2} \langle \sigma_i^z(t) \sigma_j^z \rangle_\psi. \end{aligned}$$

Here, $|\psi\rangle$ is assumed to be in the σ^z -eigenbasis. The sign in the above calculation can be immediately obtained from $|\psi\rangle$. Computing the above probability within a constant additive error suffices to yield a valid reduction to the output probabilities of quantum circuits. We are interested in the case where

the circuit C_t is given by the time evolution e^{itH} for some Hamiltonian H .

The definition of the DSF is given for continuous time (Eq. (2)), but quantum simulators (and also classical simulations) need to discretize time, as the measurement protocols proposed cannot continuously measure $C_{i,j}^{z,z}(t)$, but require a fresh preparation for each point in time. In the following we show that while this discretization leads to errors, they are bounded.

C. The discretization error

Notice that there will always be an error from the discretization of time. However, this can be bounded: For any differentiable function f we can use the mean-value theorem to obtain

$$|f(t + \delta t) - f(t)| \leq \left| \max_{t' \in [t, t + \delta t]} \partial f(t') \right| \delta t. \quad (21)$$

For $C_{i,j}^{z,z}(t) = \langle \sigma_i^z(t) \sigma_j^z \rangle_\psi$, we have

$$\begin{aligned} |\partial_t C_{i,j}(t)| &= |\langle \psi | \partial_t (\sigma_i^z(t) \sigma_j^z) | \psi \rangle| \\ &= |\langle \psi | \partial_t (e^{itH} \sigma_i^z e^{-itH} \sigma_j^z) | \psi \rangle| \\ &= |i \langle \psi | e^{itH} [H, \sigma_i^z] e^{-itH} \sigma_j^z | \psi \rangle| \\ &\leq L' = \text{const}, \end{aligned} \quad (22)$$

where we use the fact that we assume H to be a (geometrically) local Hamiltonian and L' is the Lipschitz constant. Thus, $H = \sum_{i=1}^r h_i$ with $r = \text{poly}(N)$ and $\|h_i\|_\infty \in \mathcal{O}(1)$ and furthermore, σ_i^z commutes with all but constantly many summands h_j . The inequality thus follows from the triangle inequality and the submultiplicativity of the operator norm. It hence suffices to choose a constantly small discretization step to bound this error. In particular, this proves that $C_{i,j}^{z,z}(t)$ is Lipschitz continuous with size-independent Lipschitz constant.

D. Hardness for a variant of the dynamical structure factor

The *discrete dynamical structure factor* is defined as

$$\tilde{S}^{z,z}(q, \omega) = \frac{1}{N} \sum_{i,j} \sum_{k=1}^M e^{-iq(x_i - x_j)} e^{i\omega(t_0 + k\Delta t)} \times \langle \sigma_i^z(t_0 + k\Delta t) \sigma_j^z \rangle_\psi, \quad (23)$$

with $\Delta t = (t_1 - t_0)/M$. Notice that this is the quantity that is usually approximated in numerical simulations. Computing the discrete Fourier-transform can be done via the *fast Fourier transform*, which runs in time $\mathcal{O}(\ln(M)M)$ for $M = \text{poly}(N)$. Hence if the correlators are BQP-hard, the discrete dynamical structure factor is as well.

We can bound the error on the continuous dynamical structure factor as well if only a finite interval of time is involved. We know that $C_{i,j}^{z,z}(t) = \langle \sigma_i^z(t) \sigma_j^z \rangle_\psi$ is a function with polynomially bounded Lipschitz constant. For a bounded interval

of time $[t_0, t_1]$, we consider the error that occurs by approximating the integral

$$S_{t_0, t_1}^{z,z}(q, \omega) = \frac{1}{N} \sum_{i,j} \int_{t_0}^{t_1} e^{-iq(x_i - x_j)} e^{i\omega t} C_{i,j}^{z,z}(t) dt \quad (24)$$

with step functions

$$\begin{aligned} S_{t_0, t_1}^{z,z}(q, \omega) &\approx \frac{1}{N} \sum_{i,j} \sum_{k=1}^M e^{-iq(x_i - x_j)} e^{i\omega t_0 + k\Delta t} \\ &\quad \times C_{i,j}^{z,z}(t_0 + k\Delta t) \Delta t, \end{aligned} \quad (25)$$

where

$$\Delta t = \frac{t_1 - t_0}{M}. \quad (26)$$

Integrating over the error made by the step function approximation gives us the cumulated error

$$(t_1 - t_0) L' \Delta t = (t_1 - t_0)^2 \frac{L'}{M}, \quad (27)$$

where L' is the Lipschitz constant of the function $e^{-iq(x_i - x_j)} e^{i\omega t} C_{i,j}^{z,z}(t)$. Hence, choosing M to be constant and small suffices for an approximation within arbitrarily small constant error. In essence, we have proven that $C_{i,j}^{a,b}(t)$ and $S^{a,b}(q, \omega)$ are BQP-hard in a specific sense. Furthermore, since simulations both classical and quantum require a discretization of the time axis, we have shown that the possible errors from this are well behaved and controlled.

BQP-hardness provides evidence against the existence of classical algorithms that compute dynamical structure factors in polynomial time. However, it is important to point out that this is a so-called worst-case result, i.e. it only rules out an algorithm that solves *all* cases in polynomial time. In general, subclasses of this problem are not necessarily hard in the complexity theoretic sense. For example, the time evolution of the nearest neighbour, short range, transverse Ising model is not expected to be universal for time evolution.

IV. PRACTICAL REALIZATION OF DSFS IN QUANTUM SIMULATORS

As mentioned in the previous section, several near term quantum architectures can be employed to simulate DSFs. So far we concentrated on how the previously mentioned measurement protocol can be employed to obtain DSFs, and on the complexity of this task. To assess the degree of robustness of DSFs against experimental imperfections, in Sections V and VI, we will study the transverse fields Ising model (TFIM), in the presence of those imperfections. We will consider the imperfections of two particular setups, trapped ions and Rydberg atoms [51].

Before tackling these issues, we will first give a brief introduction to the physics of the TFIM, in the absence of imperfections, for the case of short and long range interactions. The

translational invariant 1D-TFIM is defined as

$$H(J, B) = \sum_{i \in \Lambda} B_i \sigma_i^z - \sum_{i, j \in \Lambda} J_{i, j} \sigma_i^x \sigma_j^x. \quad (28)$$

The coupling parameters of the Ising term are $J_{i, j}$, and in principle can be site dependent. The strength of the magnetic field is given by B_i and in this work we will consider it uniform throughout the chain, $B_i = B$. The spin-spin interaction can take the long range form

$$J_{i, j} = \frac{J}{|i - j|^\alpha} \quad (29)$$

for analog quantum simulations in Rydberg arrays or trapped ions, where typically $\alpha \in [1, 6]$ (see Appendix A). In the case of digital simulation and optical lattices, one can study the short-range model [23] with

$$J_{i, j} = J \delta_{i, j \pm 1}, \quad (30)$$

which is exactly solvable by a mapping to non-interacting fermions [39].

While our proposal is focused on the long range model, the access to the DSF via quantum simulation for the short range case is of great importance for two main reasons. First, the short range model is much better understood than the long range counterpart, and as such, a study of its DSF can provide helpful insights on the effects of the different imperfection models, as well as on the accuracy of the measurement protocol which can be expected. Since the short range model is an easy instance of the time evolution problem, we perform a detailed study of the effects of the evolution imperfections in this case. This way we can provide sufficient understanding of the expected effects of these imperfections on the quantum simulation of the DSF. After this task is completed, we can move on to study the long range model and evaluate our practical proposal. Second, several architectures as optical lattices or Rydberg arrays can access the short range model, or the long range model at high values of α , where the system effectively behaves short range. Our study of the short range model thus provides data which can be directly used to compare with experiments on those platforms.

In the following we will describe the properties of both the short and long range TFIM and their excitations, and how those are manifested in the DSF. Please note that in this work we will study the properties of the short and long range TFIM away from criticality, for the coupling values $J = 1$ and $B = 1.4$. A study of the quantum simulation of the TFIM close to the quantum critical point is left for upcoming work.

A. Universal properties of the short range TFIM

The physics of the short range, nearest neighbour, TFIM has been studied in detail previously [39]. Here we will briefly describe the low energy excitations of the TFIM and their signature in the DSF in terms of a two kink model.

For the short range TFIM (Eqs. (28) and (30)) we can define a dimensionless parameter, $g = B/J$, and assume

$J > 0$. When $g \rightarrow \infty$, the ground state is given by a product state of spins polarized in the z -direction, $|\uparrow, \uparrow, \uparrow, \dots\rangle$, while for $g = 0$, the spins are polarized in the x -direction. When the magnetic field and Ising coupling are at a finite value, fluctuations are induced in the system, in the form of fermionic pseudo-particles γ . These fluctuations populate pseudo-particle momentum states with a given energy, but their nature is different depending on whether $g < 1$ or $g > 1$, with a gap closing and thus a quantum critical point at $g = 1$.

These excitations, the γ -fermions, can be seen in the spin picture as kinks over the fully polarized state, that require one spin to be flipped to the other eigenstate of $\sigma^x(\sigma^z)$ when $g < 1$ ($g > 1$). At the same time, once a spin is flipped, it is free to move along the chain without further energy cost. Thus, each one of those particles has a given energy, ϵ_k , and momentum k . Since a spin flip is required to generate the excitation, the energy ϵ_k is greater than zero, indicating that the ground state of the TFIM has no kinks, i.e., the ground state corresponds to the fermion vacuum. As such, we can find that the spectrum is gapped, and the exact solution of the short range TFIM yields a gap $\Delta = 2J|1 - g|$ [39], which vanishes at $g = 1$. The case of interest in this work is $g > 1$, where a flipped spin can move around the lattice and create a domain. The walls of this domain can be regarded as the kinks (or equivalently, the γ -fermions) that interpolate between the two possible ground states connected by the \mathbb{Z}_2 symmetry of the model. When a domain is formed, the domain walls or kinks behave as the free fermionic particles, that propagate through the chain. Since to create a domain we need at least two kinks (particles), the first contribution to the excitation spectrum will come from the two particle states, which will be described by their energy and momenta, $E = \epsilon_{k_1} + \epsilon_{k_2}$ and $k = k_1 + k_2$. For a fixed k , the values of k_1 and k_2 can be chosen arbitrarily, which generates a continuum of excitations.

The spectrum of excitations will manifest in the dynamical structure factor: studying the longitudinal xx -structure factor, $S^{xx}(q, \omega)$, we observe the gap, and the continuum of excitations (the so called two particle continuum) that corresponds to the two particle states we mentioned previously. This observations have been previously shown, both numerically [52] and experimentally via neutron scattering [33]. In Fig. 2 we show the xx -DSF for the short range TFIM, as obtained from our free fermionic calculation for $J = 1$ and $B = 1.4$, for 50 sites. We clearly observe the two particle continuum which characterizes the low energy fluctuations, as well as the excitation gap at the point $q = 0, \omega \sim \pi/4$ (in units of J).

B. Long range TFIM

Now we can concentrate on the case which is our test of a practical application: the investigation of *how quantum simulators can measure the DSF of the long range transverse field Ising model for system sizes beyond those reachable by state of the art classical algorithms*.

Models with these kind of long range interactions present considerable challenges to numerical studies. The long range

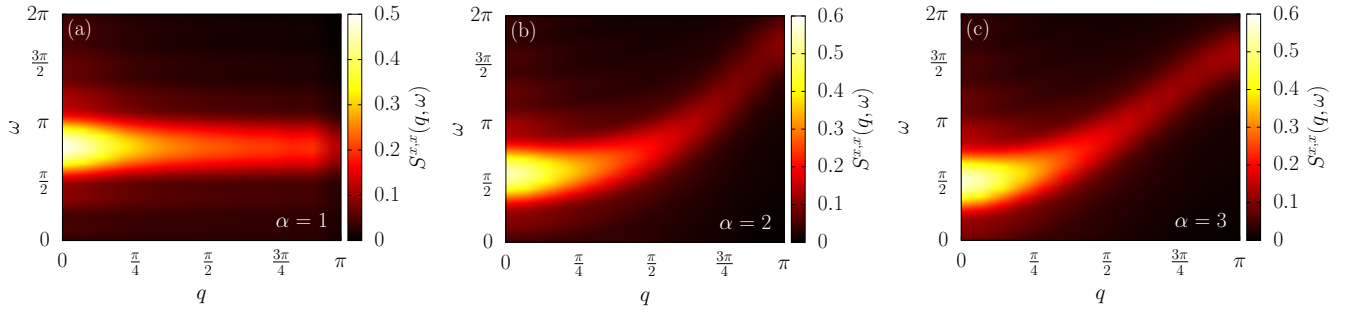


Figure 4. *Dynamical structure factor for the long range transverse field Ising model, for the cases $\alpha = 1$ (a), 2 (b), and 3(c).* For the case $\alpha = 1$ we see that the DSF does not vary in frequency, which is a possible signature of excitation confinement, in accordance with Refs. [35, 53]. For $\alpha > 2$ the two particle continuum is noticeable, and the gap is lowered. As the value of α is increased, the interactions become shorter range, and the gap approaches the value for the short range model. Accordingly, the continuum changes shape, from the absence of ω dependence for $\alpha = 1$ towards the cosine form at $\alpha = 3$. This cosine shape corresponds to the short range TFIM, obtained in the limit $\alpha \rightarrow \infty$. For comparison with the short range TFIM please refer to Fig. 2.

interactions severely constrain the system sizes which can be studied with exact diagonalization techniques based on sparse matrices. Furthermore, studies of these systems employing finite size MPS based techniques are affected by severe finite size effects arising from the entanglement cutoffs required by these approaches. Recently, however, there has been success in studying the statics of long range models employing MPS algorithms, which directly act in the thermodynamic limit, such as iDMRG [54, 55]. These techniques still employ a distance scale cutoff in their approximation to the long range interactions, but the results obtained with these algorithms describe the qualitative features of long range models reasonably well.

At the same time, several algorithms which can time evolve an MPS with long range interactions have been proposed [56, 57] to study the long range TFIM [58]. With the advent of these new techniques, and the state of the art of quantum simulators capable of implementing long range TFIM, the question of whether the DSF of this class of models can be accessed with these experimental architectures naturally arises.

Unlike the short range model which has been thoroughly studied in the past, much less is known about the long range TFIM. Recent studies [36, 38, 59] concentrate on the entanglement growth and the spread of correlations in this model as a function of the interaction length, α , or in the thermalization of different initial states under this Hamiltonian [37]. Analyzing the light cones and possible Lieb-Robinson like bounds in the long range TFIM at zero temperature, these studies separate the dynamical behaviour of this model in three regions. For $\alpha > 3$ a well defined light cone can be observed, where the correlations propagate with a constant Lieb-Robinson velocity and decay algebraically outside of the light cone with an exponent which depends on α . In this regime, the system obeys the generalized Lieb-Robinson bound [60], and the behaviour of the system mimics that of a short range model. Via semi-classical arguments, the dispersion relation of excitations in the ground state (what we study here via the DSF) is found to approximately be a cosine, which coincides with the short range behaviour. From this we can say that, for quantum

simulator measurements in the presence of the imperfections studied in this work, the behaviour of the DSF in the regime $\alpha > 3$ is expected to be very close to the behaviour of the short range model. On the other hand in the range $1 < \alpha < 3$ a broad light cone is observed, with correlations leaking out of it and an excitation dispersion which is bounded. This case is of special interest in this work, since trapped ion experiments can implement long range TFIMs in this range, but also given that it has recently been shown [35, 53, 61] that in this regime the long-range interactions introduce an effective attractive force between a pair of domain walls, while a two kink models is still a valid description. This attractive force confines the excitations in bound states analogous to the confinement of mesons in high energy physics [35, 53, 61]. Since this exotic physics can be probed studying the confinement signatures in both the unequal time correlators and DSFs, our work opens the door to the study of these effects in quantum simulators. Finally we mention that for $\alpha < 1$ the light cone completely disappears and a virtually instantaneous spread of correlations is observed. In Fig. 4 we show the DSF of the long range TFIM, as obtained numerically from a full exact diagonalization of a system of 14 spins at zero temperature, for the interaction lengths $\alpha = 1$ (a), 2(b), and 3(c). In these figures we see that for $\alpha = 1$ the DSF shows no ω dependence, which hints at the possibility of excitation confinement [35, 53, 61] being evidenced through the DSF. For $\alpha > 2$ the ω dependence is recovered, slowly approaching the short range behaviour as α is increased, in which the two particle continuum has the form of a cosine. Please note that unlike previous reports, here we observe the signatures of confinement in equilibrium, which is a necessary condition for the measurement of DSFs via the protocol proposed in this work. In view of these different regimes, we will study the long range TFIM for several values of α in the range $1 < \alpha < 6$ in the presence of the same imperfections we will consider for the short range model. We will contrast the different behaviour for different α , and also study the effects of these imperfection models on the DSF as a function of size, to ensure a controlled experimental scaling.

C. Error models

In Sections V and VI we will describe how the different experimental imperfections arise in the architectures considered in this work, but here we will briefly describe how those imperfections modify the TFIM Hamiltonian. As mentioned previously, three basic ingredients are needed to simulate DSFs on near term devices: First, we need to be able to *prepare* the ground state of the target Hamiltonian in a controlled way, and ideally with as high a state fidelity as possible. Second, we need to be able to control the *time evolution* of the system, in such a way that the physics we desire to investigate is not severely mitigated by experimental imperfections. And finally, we want to employ the proposed *measurement* protocol to determine the unequal time Green functions. Every one of these steps carries their own imperfections which we will consider separately.

For the *preparation* imperfections we will study the effect of measuring DSFs when the prepared state is close to, but not exactly, the ground state. In other words, we will prepare a state vector $|\psi_\sigma\rangle$ such that the fidelity of this state with respect to the ground state is smaller than one, $F = \langle\psi_\sigma|\psi_0\rangle < 1$. The measurement protocol is not modified by this imperfection model, such that even if the prepared state is not the ground state, we can still recover the retarded Green's function. If the fidelity of the prepared state is sufficiently high, we expect (and indeed we will show) that the DSF can still be confidently recovered via Eq. (10).

In the case of *evolution imperfections* we will study three fundamental effects over the TFIM Hamiltonian. In the first case, we will study how a time dependent modulation of the Ising couplings affects the DSF. In this case the Hamiltonian couplings are modified to be time dependent and of the form

$$J_{i,j} = \frac{J(0)}{|i-j|^\alpha} (1 + A \sin(\omega t)) \quad (31)$$

for the long range model, and similarly for the short range model:

$$J_{i,j} = J(0)(1 + A \sin(\omega t))\delta_{i,j\pm 1} \quad (32)$$

where $J(0) = J$. We will study several modulation amplitudes, $A = 0.01, 0.05, 0.1$, and 0.5 , and different frequencies ω between 0.05 and 25 .

We will also study the case of random interactions and magnetic fields, related to lattice imperfections. In these cases the Hamiltonian takes the form in Eq. (28), but for the case of random interactions the Ising couplings take the form

$$J_{i,j} = (J + A\xi_{i,j})\delta_{i,j\pm 1} \quad (33)$$

for the short range or

$$J_{i,j} = \frac{J + A\xi_{i,j}}{(i-j)^\alpha} \quad (34)$$

for the long range models. In the case of random transverse fields

$$B_i = B + A\xi_i. \quad (35)$$

In all cases ξ is drawn at random independently at each site from the uniform distribution on the interval $[0.0, 1.0)$ with $A = 0.01, 0.04, 0.1$, and 0.4 . We employ between 50 and 100 disorder realizations per data point.

We numerically study the effect of these imperfections. We calculate the DSF for both short and long range models in the clean case, as well as in the presence of the different imperfections. For the short range model we employ free fermionic techniques, since the Hamiltonian is integrable, this allows us to study the DSF for systems up to $L = 50$ sites. On the other hand, the long range model breaks integrability, and we resort to a time evolution study employing full exact diagonalization techniques. The memory requirements are thus increased for the long range model, as such the system sizes we can reach are greatly reduced in comparison to the short range model. For the study of the long range model, we reach system sizes up to $L = 14$ sites. In both cases, the time evolution is done in an open boundary chain, for a time $t \in [0, L/2]$. We point out that for the experimental imperfection regarding the measurement protocol, the major contribution to the error comes from statistical errors. We have not studied this imperfection in detail, since it is well established that this type of errors decrease as $1/\sqrt{n}$ with n the number of samples, and as such it is clear that the experiment needs to be performed multiple times to decrease statistical errors.

V. EFFECT OF EXPERIMENTAL IMPERFECTIONS ON THE DSF OF THE SHORT RANGE TFIM

Our objective in this section and the next is to demonstrate that the qualitative and quantitative features of the DSF for both the short (Sec. V) and long (Sec. VI) range TFIM can be recovered from a quantum simulation even in the presence of experimental imperfections. First, in Section V we will study how the state preparation can affect the DSF, by studying the effects of a non-adiabatic preparation. Afterwards we will study how imperfections in the evolution arising from the lack of complete control over Hamiltonian parameters can affect the output of the experiment. Finally, in Section VI, we will show how these same measurement imperfections can alter the DSF of the long range model, as well as show the scaling properties of the experiment.

In essence, to phenomenologically and briefly summarize the results shown in Sections V and VI: We show that, at the experimental levels of control present in state of the art architectures, the errors which would be produced in a measurement of the DSF for both short and long range TFIM are small, and one can trust both the qualitative and quantitative results of such experiment. Since the overall behaviour of the DSF is what gives one information about low energy excitations of a given system, and how they behave, the errors in Sections V and VI show that, at the current level of experimental control (when our imperfection parameter is set below 5%), the DSF is well behaved. Thus, the overall form of the DSF does not change and one can safely extrapolate, from a quantum simulation via the DSF, what some of the low energy excitations of a given model are, and what their behaviour is. At higher val-

ues of imperfections, the behaviour naturally changes, but we know this is due to the fact that all these imperfection models lead to different physical phenomena, and this is observed as changes in the DSF. We leave the study of these strong levels of imperfections to future work, but they already point out interesting phenomena which can be also probed in quantum simulators via the DSF and employing the same measurement protocols we propose here.

A. Quantifying imperfections

To assess what the effect of experimental imperfections is on the DSF we will analyze two particular quantities based on the absolute error of the DSF. We define the absolute error as

$$\Delta S(q, \omega) = |S^{x,x}(q, \omega) - \tilde{S}^{x,x}(q, \omega)|, \quad (36)$$

where $S^{x,x}(q, \omega)$ is the DSF obtained from the exact solution of the TFIM in the absence of imperfections. $\tilde{S}^{x,x}(q, \omega)$ is the DSF obtained from the exact solution with various perturbations in the Hamiltonian, arising from the different imperfection models. If we integrate over frequency (reciprocal space) we obtain the average error in reciprocal space (frequency),

$$\begin{aligned} \Delta S(q) &= \frac{1}{N_\omega} \sum_{\omega} \Delta S(q, \omega), \\ \Delta S(\omega) &= \frac{1}{L^2} \sum_q \Delta S(q, \omega), \end{aligned} \quad (37)$$

where N_ω is the number of frequencies, which depends on the discretization of the time evolution, and L is the system size. We show the average error for different imperfection models in the appendix. The maximum of the absolute error, for fixed ω or q , will be denoted by

$$\begin{aligned} \max_q [\Delta S(q, \omega)], \\ \max_\omega [\Delta S(q, \omega)]. \end{aligned} \quad (38)$$

These errors can be understood in the following way: Eq. (36) is the absolute error of the DSF when imperfections are considered. If one makes a cut on the absolute error at a given value of reciprocal space, q , and integrates it over frequency, one obtains the frequency integrated error at that q , $\Delta S(q)$. This is equivalent for cuts at a given frequency, ω , to obtain the reciprocal space integrated error $\Delta S(\omega)$. If, on the other hand, one selects the maximal error at that value, one obtains the maximal errors shown in Eq. (38). The study of the imperfections in this way allows us to account for the effects in frequency and reciprocal space separately. We know what the overall shape of the DSF for the short and long range TFIM is, as shown in Figs. 2 and 4. If the imperfection models do not change the DSF, then these errors should be small and flat over the entire q and ω range. On the other hand, if these errors are not small, we can assess what their effect is on the DSF by studying the shape of the quantities given in Eqs. (37) and (38). For example, if one of these imperfection

models were to close the gap, we would see errors towards small frequencies, but not on q -space. On the other hand, if the two particle continuum were to completely disappear or change shape, we would see errors over the entire frequency axis and at different q values, depending on the change in the continuum.

Since the Fourier transform is performed as data-processing over the correlators, we will compare the error of the DSF to the error in the correlators, as to assess the robustness of the Fourier transform. The error in the correlators, and the average and maximum over space (where space is indicated as $r = i - j$) are defined as

$$\Delta C_r(t) = |C_r^{x,x}(t) - \tilde{C}_r^{x,x}(t)|, \quad (39)$$

$$\Delta C(t) = \frac{1}{L^2} \sum_r \Delta C_r(t), \quad (40)$$

$$\max_r [\Delta C_r(t)]. \quad (41)$$

Finally, to determine the scaling properties of the long range model, we will study the integrated DSF error ΔS as a function of size and of the range of the interactions α where the integrated error is given by

$$\Delta S = \frac{1}{N_\omega} \frac{1}{L^2} \sum_{\omega} \sum_q \Delta S(q, \omega). \quad (42)$$

B. Influence of state preparation imperfections on the DSF

In Section IV we stated that we will concentrate on two architectures, trapped ions and Rydberg atom arrays. Both of them can prepare the initial state via an adiabatic evolution of the Hamiltonian from a high field phase, where the state is fully polarized in either the z - or x -direction (depending on the initial field value), and then evolve it towards the desired parameter values. Furthermore, trapped ions can prepare it through quantum approximate optimization techniques [43]. For a spin system, the adiabatic regime is given when the evolution time is much larger than the inverse gap, in the particular case of the TFIM this means that the adiabatic preparation time τ_Q has to be such that $\tau_Q \gg 1/(4|J - B(t)|^2) + \xi$, where ξ is the finite size contribution to the gap. We will study here how the DSF is affected by different evolution times, when the final field value is far away from the quantum critical point, $J = 1$ and $B = 1.4$.

Adiabatic time evolution. The question that motivates us is how the features of the DSF change when the system is prepared for a time τ_Q (the preparation time) from an initial polarized state, (which corresponds to the $B \rightarrow \infty$ limit) to the final state $B = 1.4$. In principle, when requiring an adiabatic evolution, there exists a bound on τ_Q which depends on the size of the gap of the system. In particular, in the thermodynamic limit this preparation time diverges when one approaches the quantum critical point. For a finite system, it can be shown that the finite size gap destroys the divergence, and a finite bound on the preparation time can be obtained [62, 63]

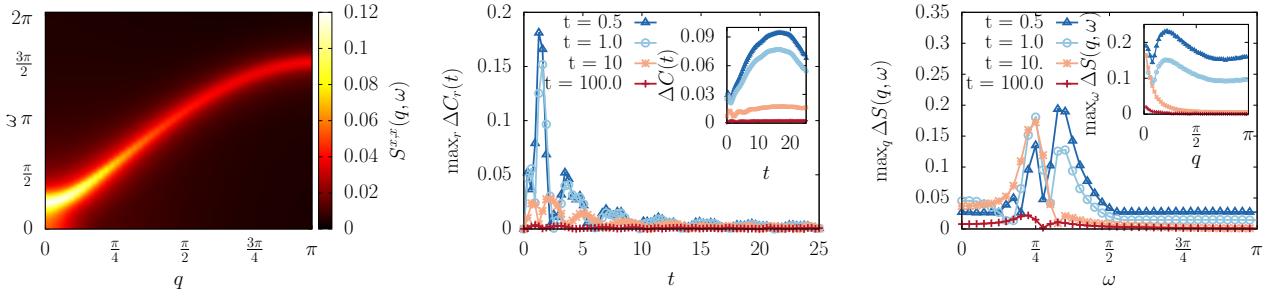


Figure 5. *Effect of finite preparation times τ_Q on the DSF of the short range TFIM.* We show numerical results for the DSF and unequal time correlation functions of the short range TFIM subject to different preparation times $\tau_Q = 0.5, 1, 10, 100$. (*Left panel*) DSF of the TFIM for a preparation time $\tau_Q = 0.5$. This can be directly compared to the imperfection free case shown in Fig. 2. Qualitatively, we observe that the overall intensity has decreased, and the low ω sector has broadened. (*Middle panel*) Cuts of the absolute error for the unequal time correlation function, depicted for a quantitative comparison. We observe that at short preparation times $\tau_Q = 0.5$ and $\tau_Q = 1$ we find significant deviations of local correlation functions at short times, which continuously decay over time t . The inset shows the averaged error in the correlators, which indicates that the deviation seen in the maximal error persists, and in fact increases, at all times on the level of uniform real-space average. The decay in the maximal error can be understood in terms of the propagation of the errors within the Lieb-Robinson cones as discussed in the main text. (*Right panel*) Cuts in frequency and reciprocal space (inset) of the DSF absolute error. We quantitatively verify the intuition given by the left most panel. The DSF indeed encodes the correct physical information despite the deviations in real-space and the deformation of the low ω sector. The low error intensity away from the point $\omega = \pi/4$ and $q = 0$ indicate that the gap remains open for the lowest imperfection level. The concentration of errors is located around the gap. The absence of errors for long preparation times at $q > 0$ and $\omega > \pi/4$ indicate that the two particle continuum is not affected by these preparation times, while for values $\omega < \pi/4$ a small but non-zero error remains for short times, indicating that the shape of the DSF close to the gap is broadened.

within which the evolution remains adiabatic. Experimentally, whether such times can be realized depends on the particular properties of the experiment itself, and on the level of control that can be achieved over the preparation parameters.

Considering our previous discussion, it is imperative that we study how the properties of the DSF change when the preparation is not adiabatic. In this case, if the preparation time is not large enough to be in the adiabatic regime, the quantum simulation can still be able to obtain results which are close to the physics that one desires to study. This can be understood, and generalized to preparation protocols beyond adiabatic evolutions, if one thinks about the fidelity of the prepared state. If the fidelity is high, then the properties of the DSF evaluated over the prepared state will remain close to the properties of the DSF evaluated over the exact ground state. Furthermore, if the preparation evolution is not adiabatic, but does not surpasses the quantum critical point, then there exists a time interval in which the transition probabilities towards excited states is sufficiently small, such that the main contribution to the state of the system is the ground state [62–66]. At the parameter values studied here, where the excitations are kinks corresponding to domain walls (and the ground state corresponds to the vacuum of kinks), the fidelity of the prepared state F can be thought of as the probability that no extra defects have been created during the preparation. In this sense, if at a certain field value the low energy states naturally have a given number of kinks, we want that our preparation will not create any additional ones, which implies a prepared state fidelity close to one, thus safeguarding the integrity of the DSF calculated over such a state. Ref. [63] calculates the fidelity of the final state with respect to the vacuum of excitations for a linear ramp, effectively probing the probability that

no excitations have been created during the preparation, even if the quantum critical point has been crossed. The authors find that the fidelity takes the form

$$\ln(1 - F) = -\pi\Delta^2/(4B/\tau_Q). \quad (43)$$

With this in mind, we can simply ask the question of *how large does τ_Q need to be such that $F \sim 1$, and what are the effects on the DSF when $F < 1$?*

We quantify the robustness of the DSF to preparation imperfections employing the error measures shown in Section V A. For this we numerically calculate the DSF of the short range TFIM, including an initial state preparation. We prepare the state by a total time τ_Q , starting with the field at $B_{\text{ini}} \rightarrow \infty$ and finishing at $B_{\text{final}} = 1.4$. The total time is partitioned into N small time steps $\Delta T = \tau_Q/N$. We sequentially evolve by time ΔT , where the magnetic field is linearly ramped up from 0 to the desired value B_{final} .

The adiabatic evolution has been performed for different evolution times, ranging from $\tau_Q = 0.005$ to $\tau_Q = 3000$. In Fig. 5 we show the error analysis for preparation times $\tau_Q = 0.5, 1, 10$, and 100 . Following the calculations of Ref. [63] we estimate that the fidelity of the prepared state (assuming no other error sources) will correspond to $F \sim 0.043$ for a preparation time of $\tau_Q = 0.5$, to $F \sim 0.59$ for $\tau_Q = 10$, and $F \sim 0.99$ for $\tau_Q = 100$. Our numerical error analysis of the DSF and correlators coincides with these fidelity estimates. We tackle the DSF first: in the left most panel of Fig. 5 we show a typical DSF for a preparation time $\tau_Q = 0.5$, and in the right most panel we show the maximum error of the DSF over frequency (main figure) and reciprocal space (inset). For $\tau_Q = 100$ the maximum error is below 5% and mostly flat over the entire (ω, q) space, indicating that at this parameter

values this preparation time is enough to not excite the system further and obtain an accurate DSF. This can be confirmed by comparing the left most panel of Fig. 5 and Fig. 2. From these figures we notice that the discrepancy in the DSF between the exact case and the one studied in this section appears around the point ($q = 0, \omega = \pi/4$) (and in a small measure for $\omega < \pi/4$). This point corresponds to the position of the gap in the clean case, for the parameter values studied here. Even for the worst case shown, $\tau_Q = 0.5$, most of the error is constrained around the gap, indicating that the main contribution to the error in the DSF is a qualitative change in the overall broadness of the low q low ω sector. Even though this broadness is clearly observed for the shortest preparation times, the overall shape of the DSF does not change (as is seen in the left most panel).

In the case of unequal time correlators, shown in the middle panel of Fig. 5, we see that the maximal (average in the inset) error in this case, for $\tau_Q = 100$, is also below 5% (1%), but we can see how the average error increases over time. While looking at the correlators directly could also be a way to study the ground state fluctuation of the system (given that the effect of the imperfections is small), the interpretation of the data as a function of time can be much more challenging, especially for long times. This can be understood by considering the propagation of errors as a function of time, which takes place with a maximal velocity consistent with the Lieb-Robinson bounds. We show in Fig. 13 in Appendix C the propagation of errors in the correlators as a function of time, and the light cone consistent with the Lieb-Robinson behaviour expected in this model. With this in mind, we can note that the Fourier transform leading to the DSF allows one to understand and deal with the errors arising from this imperfection model in a much more simple way in comparison to the case of unequal time correlation functions. Furthermore, since the DSF includes all the spacial and temporal data of the correlators, and the errors are controlled and can be well understood, we can say that even though the imperfection levels studied here do not induce big errors in correlators or the DSF, the minimal change in the qualitative features of the DSF as well as the simplicity of the data analysis, indicates that the DSF is an optimal and robust quantity to study in the presence of these type of imperfections.

C. Influence of evolution imperfections on DSF

In trapped ions architectures, the transverse field and Ising interactions are engineered by applying off-resonant laser beams (see Appendix A). In particular the spin-spin interactions are created by coupling the spin states to the normal modes of motion of the ions by these laser beams [67, 68], obtaining a coupling strength directly proportional to the Rabi frequency of the ions. The lasers employed present intensity and phase oscillations which can be currently controlled up to a certain threshold [69]. This induces a variation of the Rabi frequencies across the chain, and can also induce the presence of other vibrational modes in the effective spin-spin interaction, resulting in interactions which are not necessarily

uniform along the chain and over time.

Globally fluctuating Ising coupling - Laser intensity fluctuations on trapped ion devices. We will study the particular case in which the intensity fluctuations of the lasers directly induce periodic fluctuations of the Rabi frequencies, and as such, periodic fluctuations of the spin-spin interactions (see Appendix A). We will model these evolution imperfections by modulating the Ising coupling as in Eq. (32), with different amplitudes A and different frequencies w .

In Fig. 6 we show the error analysis of the DSF and unequal time correlation functions for the case of modulated Ising couplings. We have studied a range of frequencies from $w = 0.05$ to $w = 25$ and intensities in the range $A \in [0.01, 1]$. Here, where $J = 1$, a coupling intensity $A = 0.01$ ($A = 1$) correspond to a 1% (100%) fluctuation in the Ising coupling. Current experimental capabilities can constrain these parameters within the 1% threshold [70].

At the parameter values studied, the effects are mainly noticed as a function of the coupling A . Concentrating on the error of the DSF shown in the left and right most panels of Fig. 6, we see that even the lowest coupling studied $A = 1\% = 0.01$ can induce a maximal error of 15% in the DSF. The error is concentrated, as in the case of preparation imperfections, around the maximum of the DSF, we have $q = 0$ and $\omega \sim \pi/4$ for the smallest intensity. Already for $A = 0.05$ we see that small broad peaks appear for $\omega > \pi/4$, while for $A = 0.5$ the shape of the DSF is changed, as indicated by the large errors all along the frequency axis in the middle panel of Fig. 6. This can be understood by looking at the left most panel of Fig. 6, which exhibits the DSF for a 10% modulation, and comparing it with Fig. 2. Besides the overall decrease in intensity, the low frequency shape of the two particle continuum has changed, giving the maximum in the right most panel of Fig. 6 at $\omega = \pi/4$. There is also an increase of intensity at small q for a range of frequencies up to $\omega = \pi/2$, which coincides with the maxima in the right most panel at these same frequencies.

In the case of the unequal time correlators, the middle panel of Fig. 6, the error intensity is much higher, with a maximum of 65% at small times which decays to close to zero at long times, for all amplitudes except $A = 0.5$. While at first it seems that the error disappears at long times, this is an artefact generated by the error propagation of the correlators. As we show in Appendix C, the errors propagate in a Lieb-Robinson cone, with an interference pattern within this cone. This interference pattern gives a maximal error which ranges between zero and 0.05. As such, even if the maximal error is small within the cone, there is an overall error which increases (monotonically at small amplitudes, in an oscillatory fashion at higher amplitudes) with time, which indicates that long measurement times lead to the propagation of errors and to an, in average, very large inaccuracy in the correlators. As for the case of preparation imperfections, the error in the correlators can make for a hard determination of the propagation of excitations through the system. The DSF allows us to study these effects even in the presence of imperfections, given that the errors in this quantity are localized close to the maxima, and the overall shape of the two particle continuum

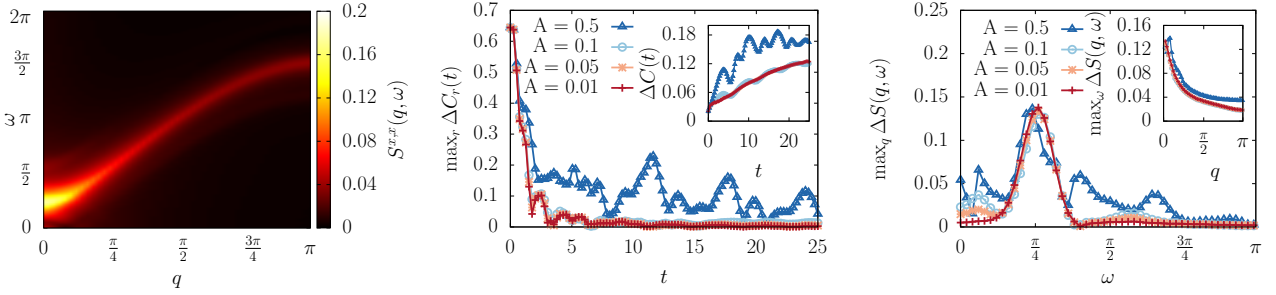


Figure 6. *Effect of globally fluctuating Ising couplings on the DSF of the short range TFIM.* We show numerical results for the DSF of the short range TFIM subject to the imperfection model (32) with Ising couplings harmonically modulated for amplitudes $A = 1, 5, 10$, and 50% . (Left panel) DSF of the TFIM for an Ising coupling modulated by $A = 10\%$. This can be directly compared to the imperfection free case shown in Fig. 2. Qualitatively, we observe that the overall intensity has decreased, and the low ω sector has broadened. But the gap and the two particle continuum remain, even with this high level of modulation. (Middle panel) Cuts of the absolute error for the unequal time correlation function, shown for quantitative comparison. We see that at short times there are significant deviations of the local unequal time correlation functions which rapidly decay over time for all modulation intensities except 50% . The inset shows that this deviation persists, and in fact increases, at all times on the level of uniform real-space average. (Right panel) Cuts in frequency and reciprocal space (inset) of the DSF absolute error. We quantitatively verify the intuition given by the left most panel. The DSF indeed encodes the correct physical information despite the deviations in real-space and the deformation of the low ω sector. The low error intensity away from the point $\omega = \pi/4$ and $q = 0$ indicate that the gap remains open for the lowest imperfection level. The broadness of the maxima in the frequency cuts indicate that even though the gap is still open, it is slightly shifted with respect to the exact solution of the short range TFIM. The inset shows that the effect over momentum space does not decay to zero, and for high momenta the maximal error is stabilized to a value greater than 0. Looking at the left most panel we can understand this non-zero error at high momenta as coming from the lower intensity in the DSF signal in comparison to the clean solution, and not from a deformation of the two particle continuum.

is minimally changed for small intensities of the fluctuating coupling.

It has to be pointed out, that for slightly higher intensities of the fluctuating coupling, even for $A = 5\%$, small changes in the DSF are seen both in the frequency and reciprocal space axis. This indicates that this imperfection model has to be dealt with carefully in an experimental setup, as small increases in A can lead to appreciable effects in both the DSF and the unequal time correlators, and the possible bounds on A and w need to be dealt with carefully [71]. Nevertheless, for an experimentally achievable value of $A = 1\%$, the deformations of the DSF are minimal, and a good definition of the two particle continuum and gap can be obtained (see Fig. 11(b) in Appendix C).

As a final point in this section, we want to remark on the fact that the possibility of engineering oscillatory Ising couplings via the laser fluctuations or other methods, combined with site resolved spectroscopy offers the chance to study non-equilibrium, Floquet type, phenomena based of periodically driven long and short range systems in the near term quantum devices studied here.

Lattice imperfections. Many experimental imperfections can lead to randomness in the parameters of the prepared Hamiltonian. In particular, the finite temperature present in the experiments induces fluctuations in the atomic positions which can lead to fluctuations in the interaction energy between atoms from shot to shot. At the same time, the global Rabi frequency can also fluctuate from shot to shot, which induces fluctuations in the Ising interaction in the case of a Rydberg atom setup, or in the transverse field for the case of trapped ions (see Appendix A).

The Rydberg atom setup is based on the combination of

strong, controllable interactions, with atom-by-atom assembly of arrays of trapped cold neutral Rb atoms. A two-photon process couples the ground state vector $|g\rangle$ to the Rydberg state vector $|r\rangle$ of the trapped atoms via an intermediate state, employing lasers with single photon Rabi frequencies. The interaction between the atoms can be varied by coupling them to different Rydberg states or changing the distance between them. Employing a spin-dependent optical dipole-force, spin-spin interactions can be generated [24, 25] (see Appendix A). Since the Rydberg atoms are not in the ground state once in the local trap, and the experiment is carried at a finite temperature, fluctuations in the atomic positions for each atom in each cycle of the experiment are introduced [24, 25], which will affect the Ising interaction (see Eq. (A2) in Appendix A). In a typical experiment the lattice spacing is chosen around $6\mu m$, and the typical fluctuation of the position is of around $128nm$, this induces a change in the Ising coupling between 0.1% and 0.2% [24, 25].

In a setup where ions are trapped by a linear Paul trap, a 1D spin-1/2 Ising system in the presence of a transverse field can be engineered [27] by the hyperfine "clock" states of these ions (see Appendix A). The transverse field and spin-spin interactions can be obtained applying off-resonant laser beams [67, 68], and in particular the transverse field is generated by uniformly illuminating the ion chain with two Raman laser beams whose difference in frequency is tuned to the hyperfine splitting. This process induces Rabi oscillations in the ions, with a frequency Ω_i , where i indexes the ion site on the lattice. These oscillations are seen as AC Stark shifts in the spin states, effectively acting as a magnetic field. In this architectures, the Rabi frequency Ω_i can vary across the chain from shot to shot, and other vibrational modes can also contribute

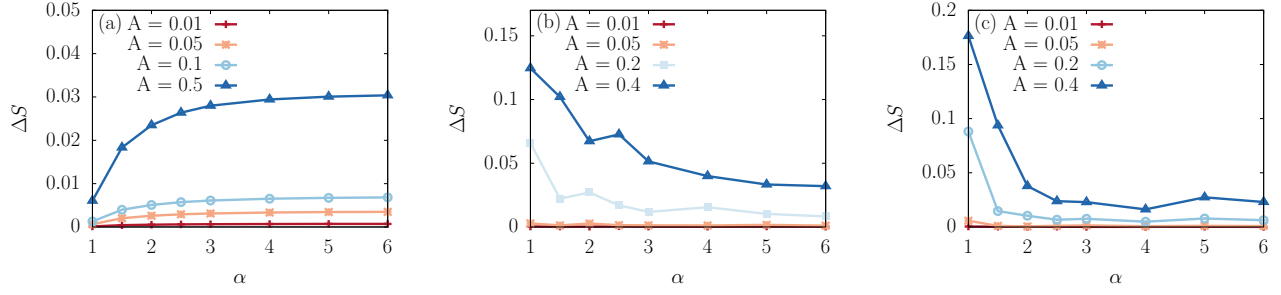


Figure 7. *Effect of experimental imperfections in the DSF for the long range TFIM.* We plot the average error, ΔS as a function of the interaction range, α , for $L = 14$ sites. (a) Effects of laser intensity fluctuations, where the Ising couplings are harmonically modulated, Eq. (31). These fluctuations increase as α is increased, with the error being minimal at $\alpha = 1$, within the confined phase, and saturating at $\alpha > 3$, when the system approaches the short range TFIM. (b), (c) Effect of lattice imperfection for random fields (b), and random interactions (c). For both these cases the effect is the same, the DSF is highly susceptible to randomness at low values of α , and it monotonically becomes more robust as α is increased, recovering the short range behaviour for $\alpha \rightarrow \infty$. A physical interpretation of the effect on the excitations of these imperfection models on the DSF is beyond the scope of this work, as the presence of excitation confinement in the long range model has been proposed recently [35, 53, 61]. We suggest that a detailed study of these imperfection models on long range systems as the one studied here can be highly rewarding given the availability currently present to study these systems in quantum simulators, but also due to the exotic excitation confinement present in long range systems. From our results we observe that while the errors depend on the value of α , these imperfections lead to bounded errors. Furthermore, at the experimental levels of control currently available, the integrated error is minimal, and the overall shape of the DSF is unchanged, indicating that quantum simulators can probe the regime of interactions studied in this work, $1 < \alpha < 6$, and obtain accurate DSFs for system sizes bigger than what state of the art classical algorithms can achieve.

considerably, which can lead to interactions which are modified also from shot to shot (see Eq. (A3) in Appendix A).

The distance fluctuation in Rydberg atoms architectures can be empirically modelled as random modulations of the atom-atom distance [24, 25], while for trapped ions the Rabi frequency oscillations can be modelled as random Ising interactions from shot to shot. Taking this into account, an evolution imperfection of this kind, in a Rydberg atom or trapped ion experiment, can be modelled as a random Ising interactions as in Eq. (33). In the case of a Rydberg atom setup, the Rabi frequency is also not uniform along the chain. Since this frequency gives rise to the transverse field (see Eq. (28)), this type of evolution imperfection can be empirically modelled as a random transverse fields as in Eq. (35).

For these two cases, we show the results in the Appendix B, since they are very similar as those found for the preparation imperfections. In both cases we see that the majority of the imperfections are concentrated around the maximum of the DSF, where the gap is located. Strong random Ising interactions tend to close the gap, as can be seen in Figs. 9 and 11(c) in Appendix B. On the other hand, random transverse fields tend to open it (see Figs. 10 and 12(d) in Appendix B). In both these cases, for the experimentally tolerable imperfections of around 1%, the errors in the DSF and correlators are both reduced, leading to no noticeable effects in the DSF. While the errors in the correlators (Figs. 9 and 10 in Appendix B) are also small, the average error increases with time, as it was the case for the evolution imperfections. In this sense, while a study of the system's behaviour in terms of the correlators is possible, long measurement times can lead to very large errors, rendering the results analyzed purely via correlation functions highly unreliable. If one desires to study the propagation of excitations and their nature, via state of the art quantum sim-

ulators, is advisable to do it through the DSF.

We note that the regime in which randomness is large is interesting in itself, as it offers the chance to directly probe the effect of random disorder in spin chains via time dependent observables, and the DSF in particular, in near term quantum devices. In particular, the study of localization phenomena is a promising route, in particular given that this study can be directly extended to long range models, whose dynamical behaviour is currently not entirely understood in the presence of disorder. Furthermore, the system sizes that can be achieved by classical simulation techniques to study MBL effects in these systems are well below what near term quantum architectures can achieve. The reduced system sizes in classical numerical simulations render the study of MBL in long range models challenging, especially those studies based on finite size scaling [72]. While a study of MBL phenomena in long range systems via dynamical quantum simulators is beyond the scope of this work, we encourage this as a promising direction in which quantum simulators can bring a quantum leap in the achievable system sizes.

VI. INFLUENCE OF EXPERIMENTAL IMPERFECTIONS ON THE DSF OF THE LONG RANGE TFIM

In the previous section we have assessed the accuracy of a DSF measurement for the short range TFIM using quantum simulators, and have shown that the DSF is well behaved in the presence of experimental imperfections even at large system sizes. Now, we will put forward the idea that *quantum simulators can recover the DSF of long range models accurately for system sizes larger than state of the art classical simulations can treat*. To show this, we will numerically study

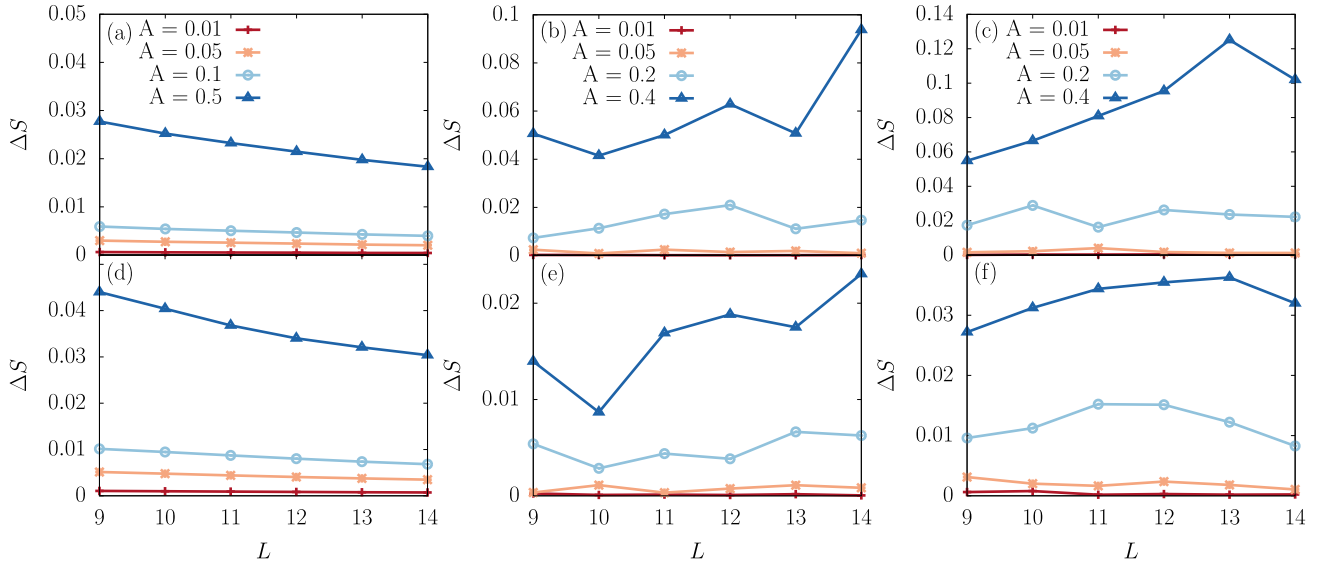


Figure 8. *Average DSF error as a function of system size for the long range TFIM.* We show the average error in the DSF, ΔS , arising from the different imperfection models. We show the numerical results for two interaction ranges. In the top panels, (a), (b), (c) we show the results for the interaction exponent $\alpha = 1.5$, while in panels (d), (e), and (f) we show the results for $\alpha = 6$. (a), (d) We show the effects of harmonically modulated Ising interactions, arising from laser intensity fluctuations. (b), (e) Average error in the DSF for the case of random interactions arising from lattice imperfections and non-uniformities of the Rabi frequency. (c), (f) Average error in the DSF arising from non-uniformity of the Rabi frequency in Rydberg atoms experiments, which translates as random transverse fields in the TFIM. For all these cases, at the experimental level of control over the different imperfections, $A < 5\%$, the error is small and constant along the whole range of sizes. When the imperfection level is reduced below 20%, it becomes negligible for all system sizes and interaction ranges. These plots show that, at the current levels of experimental control, the error remain constant and small even at the smallest size studied here, with the DSF remaining unchanged through the entire α range employed in this work. This indicates that the integrated DSF error is intensive with respect to the system sizes, and as such we expect that the scaling properties of the long range TFIM will be maintained for even bigger sizes, suggesting a good scaling of a quantum simulation to system sizes beyond what current classical algorithms can achieve.

the long range TFIM in the presence of the same experimental imperfections as for the short range TFIM. We show how the error induced by these imperfections changes as a function of the range of interactions and that it is controlled as the system size is increased.

In Fig. 4 we show the DSF in the absence of imperfections for three different values of α . In Appendix D we show the results for $\alpha = 2, 3$, and 6 . Furthermore, in Appendix E we show the heat maps for the unequal time correlations with respect to the middle of the chain, as a function of time and distance, $C_{i,5}^{x,x}(t)$, for the values $1 \leq \alpha \leq 6$ and for a system of $L = 14$ spins. In the regime $1 < \alpha < 2$ our results exhibit a particular signature in the DSF which has no ω -dependence. If one looks at the correlators for these same values of α , the spreading over space is drastically reduced, being mostly concentrated around the middle of the chain. For higher values of α remnants of this behaviour are noticed, but an ω -dependence is recovered, and the correlations slowly start to propagate. For $\alpha > 3$ we recover the cosine shaped two particle continuum, and we see a light cone in the case of the correlators. These results, especially the absence of ω -dependence for $\alpha < 2$ and the behaviour of the associated correlators, indicates that the signatures of excitation confinement, which have been recently proposed [35, 53, 61] can be observed in dynamical quantum simulators via the DSF employing our proposed method.

In Appendix F we show a typical case for the the maximal error as a function of frequency (reciprocal space) Eq. (37) (Eq. (38)) in the case of random transverse fields. There we can see that the overall behaviour of the error is very similar to that for the short range TFIM. There is a large error around the gap, with small fluctuations at other values of ω for strong imperfections. For small imperfection levels (1% – 5%) the error in the DSF is negligible, for all imperfections models, as it was found for the short range TFIM.

In Fig. 7 we show the integrated error (Eq. (42)) as a function of the interaction range α (see Eq. (29)) for the models corresponding to evolution imperfections. Fig. 7(a) show the error for the case of laser intensity fluctuations, while Fig. 7(b) and (c) show the random fields and random interactions respectively. In both cases we see two regimes, where the error drastically changes for $1 < \alpha < 3$, while it stabilizes for $\alpha > 3$. For the laser intensity fluctuations, the error monotonically increases in the first regime, and saturates in the second. On the other hand, the opposite behaviour is observed for the lattice imperfections, where the error decreases as a function of α . We remind the reader that for $\alpha > 3$ the system qualitatively behaves as the short range TFIM, following a generalized Lieb-Robinson bound, and exactly recovering the short range model at $\alpha \rightarrow \infty$.

While the errors change as the value of α is modified, at the imperfection levels present in the current architectures the

integrated error is negligible, indicating that the DSF at all values of α can be probed using these setups and the measurement would yield accurate results. Please note that the behaviour, when the errors are not negligible is also interesting since they connect to Floquet (laser intensity fluctuations), and disorder (random fields and interactions) physics, especially at small values of α , where the excitations are confined. A study of these strong effects is beyond the scope of this work, but we encourage future research in this direction.

A. System size scaling for long range models

Now we concentrate on the scaling properties of the DSF of the long range TFIM. We study system sizes ranging from $L = 9$ to $L = 14$ sites employing full exact diagonalization, and analyze how the integrated error changes with size. Since current architectures can simulate up to approximately 50 sites [24, 25], this is a playground in which the DSF can be employed to explore the potential of dynamical analogue quantum simulators. Since in the previous section we showed that the average error separates the response of the system into two well defined regimes, we will show the scaling properties of the error for one representative case of each regime, $\alpha = 1.5$ and $\alpha = 6$. In Fig. 8 we show the integrated error originating from the evolution imperfections, as a function of system size, for the two aforementioned values of α .

For imperfection levels below 10%, the integrated error is relatively constant over the full range of system sizes studied here. When the imperfection level is reduced further, to below 5% (well within current experimental capabilities), it becomes negligible for all system sizes and interaction ranges. The fact that our data suggests that the error remains constant and small at even the smallest sizes studied here, indicates that the integrated DSF error is intensive with respect to the system sizes, and as such we expect that the scaling properties will be maintained for larger chains. Furthermore, our data indicates that a dynamical quantum simulator can measure the DSF of the long range TFIM accurately, even in the presence of realistic experimental imperfections, for system sizes considerably bigger than what is currently achievable with numerical simulations, thus paving the way towards a practical quantum advantage.

VII. CONCLUSIONS

In this work, we propose the observation of dynamical structure factors as a practical application of dynamical quantum simulators. We have shown that the BQP-hardness of general local Hamiltonian time evolution is inherited by the dynamical structure factor, suggesting that its efficient classical computation might be infeasible also for practically relevant instances. In this endeavour, we build on the measurement protocol of Ref. [41] and tomographic ideas, allowing

to measure the DSF in several different quantum architectures. These architectures include those of trapped ion, Rydberg atoms, cold atoms in optical lattices, and superconducting qubits.

To emphasize the feasibility of this approach, we study the robustness of the DSF against several meaningful models of experimental imperfections for the short and long range transverse field Ising model (TFIM). Our results for the short range TFIM indicate that the overall features of the DSF are preserved when one considers state of the art setups, their associated experimental imperfections, and the current level of control over them. For the long range model, we observe that the effects of imperfections at the current experimental levels and for the system sizes studied in this work do not change the DSF. We have brought our findings into contact with signatures of the exotic physics in the long range TFIM, in particular the confinement of excitations which has been recently reported. Unlike previous studies, we observe the signatures of confinement in both the DSF and correlators in equilibrium, i.e., without the need to quench the Hamiltonian, with equilibrium being a fundamental requirement of our proposed DSF measurement protocol. Following the study of these imperfections we carry out a system size scaling, which indicates that the errors of the DSF induced by these imperfections are controlled over the whole range of sizes – remaining small and constant. This indicates that for the imperfections considered in this work, a quantum simulation experiment with system sizes considerably bigger than what state of the art classical algorithms can achieve is expected to yield accurate results. We therefore argue that the measurement of DSFs in quantum simulators provides a useful tool to assess time dependent quantities of key importance in condensed matter physics, and further place quantum simulators into the realm of quantum technological devices [73]. We hope that the present work stimulates further assessments of this quantity in other physical contexts.

VIII. ACKNOWLEDGEMENTS

M. L. B. wishes to thank Dante Kennes, Markus Heyl, David Luitz, Pedram Roushan, Pietro Silvi, Jan Carl Budich, Bela Bauer, and Thierry Giamarchi for fruitful discussions. J. E. acknowledges discussions with Holger Boche. This work has been supported by the ERC (TAQ), the Templeton Foundation, the FQXi, and the DFG (EI 519/14-1, EI 519/15-1, CRC 183, FOR 2724) and MATH+. This work has also received funding from the European Unions Horizon 2020 research and innovation programme under grant agreement No 817482 (PASQuanS). J. B. V. acknowledges funding from the European Unions Horizon 2020 research and innovation programme under the Marie Skłodowska-Curie grant agreement N 754446 and UGR Research and Knowledge Transfer Found Athenea3i.

-
- [1] H. Bethe, *Z. Phys.* **71**, 205 (1931).
- [2] E. H. Lieb and F. Y. Wu, *Phys. Rev. Lett.* **20**, 1445 (1968).
- [3] F. D. M. Haldane, *J. Phys. C* **14**, 2585 (1981).
- [4] N. M. Bogoliubov, R. K. Bullough, and J. Timonen, *J. Phys. A* **29**, 6305 (1996).
- [5] G. Ortiz, R. Somma, J. Dukelsky, and S. Rombouts, *Nucl. Phys. B* **707**, 421 (2005).
- [6] J. Dukelsky, S. Pittel, and G. Sierra, *Rev. Mod. Phys.* **76**, 643 (2004).
- [7] L. Amico, A. Di Lorenzo, and A. Osterloh, *Phys. Rev. Lett.* **86**, 5759 (2001).
- [8] R. W. Richardson, arXiv e-prints (2002), [arXiv:cond-mat/020351](#).
- [9] W. M. C. Foulkes, L. Mitas, R. J. Needs, and G. Rajagopal, *Rev. Mod. Phys.* **73**, 33 (2001).
- [10] R. M. Noack and S. R. Manmana, *AIP Conf. Proc.* **789**, 93 (2005).
- [11] R. Orus, arXiv e-prints (2018), [arXiv:1812.04011](#).
- [12] S. Aaronson, arXiv e-prints (2005), [arXiv:quant-ph/0502072 \[quant-ph\]](#).
- [13] S. Aaronson, (2009), [arXiv:0910.4698](#).
- [14] R. Ran and A. Tal, *Proc. STOC 51st Ann. ACM SIGACT Symp. Th. Comp.*, 13 (2019).
- [15] M. Marvian, D. A. Lidar, and I. Hen, *Nature Comm.* **10**, 1571 (2019).
- [16] J. Klassen, M. Marvian, S. Piddock, M. Ioannou, I. Hen, and B. Terhal, [arXiv:1906.08800](#).
- [17] D. Hangleiter, I. Roth, D. Nagaj, and J. Eisert, arXiv e-prints, [arXiv:1906.02309 \(2019\)](#), [arXiv:1906.02309 \[quant-ph\]](#).
- [18] J. I. Cirac and P. Zoller, *Nature Phys.* **8**, 264 (2012).
- [19] J. Eisert, M. Friesdorf, and C. Gogolin, *Nature Phys.* **11**, 124 (2015).
- [20] T. Fukuhara, P. Schauß, M. Endres, S. Hild, M. Cheneau, I. Bloch, and C. Gross, *Nature* **502**, 76 (2013).
- [21] T. Fukuhara, A. Kantian, M. Endres, M. Cheneau, P. Schauß, S. Hild, D. Bellem, U. Schollwöck, T. Giamarchi, C. Gross, I. Bloch, and S. Kuhr, *Nature Phys.* **9**, 235 (2013).
- [22] M. Cheneau, P. Barmettler, D. Poletti, M. Endres, P. Schauß, T. Fukuhara, C. Gross, I. Bloch, C. Kollath, and S. Kuhr, *Nature* **481**, 484 (2012).
- [23] J. Simon, W. S. Bakr, R. Ma, M. E. Tai, P. M. Preiss, and M. Greiner, *Nature* **472**, 307 (2011).
- [24] H. Bernien, S. Schwartz, A. Keesling, H. Levine, A. Omran, H. Pichler, S. Choi, A. S. Zibrov, M. Endres, M. Greiner, V. Vuletić, and M. D. Lukin, *Nature* **551**, 579 (2017).
- [25] J. Zhang, G. Pagano, P. W. Hess, A. Kyprianidis, P. Becker, H. Kaplan, A. V. Gorshkov, Z. X. Gong, and C. Monroe, *Nature* **551**, 601 (2017).
- [26] J. G. Bohnet, B. C. Sawyer, J. W. Britton, M. L. Wall, A. M. Rey, M. Foss-Feig, and J. J. Bollinger, *Science* **352**, 1297 (2016).
- [27] R. Islam, E. E. Edwards, K. Kim, S. Korenblit, C. Noh, H. Carmichael, G. D. Lin, L. M. Duan, C. C. Joseph Wang, J. K. Freericks, and C. Monroe, *Nature Comm.* **2**, 377 (2011).
- [28] S. Trotzky, Y.-A. Chen, A. Flesch, I. P. McCulloch, U. Schollwöck, J. Eisert, and I. Bloch, *Nature Phys.* **8**, 325 (2012).
- [29] P. Roushan, C. Neill, J. Tangpanitanon, V. M. Bastidas, A. Megrant, R. Barends, Y. Chen, Z. Chen, B. Chiaro, A. Dunsworth, A. Fowler, B. Foxen, M. Giustina, E. Jeffrey, J. Kelly, E. Lucero, J. Mutus, M. Neeley, C. Quintana, D. Sank, A. Vainsencher, J. Wenner, T. White, H. Neven, D. G. Angelakis, and J. Martinis, *Science* **358**, 1175 (2017).
- [30] B. Chiaro, C. Neill, A. Bohrdt, M. Filippone, F. Arute, K. Arya, R. Babbush, D. Bacon, J. Bardin, R. Barends, S. Boixo, D. Buell, B. Burkett, Y. Chen, Z. Chen, R. Collins, A. Dunsworth, E. Farhi, A. Fowler, B. Foxen, C. Gidney, M. Giustina, M. Harrigan, T. Huang, S. Isakov, E. Jeffrey, Z. Jiang, D. Kafri, K. Kechedzhi, J. Kelly, P. Klimov, A. Korotkov, F. Kostritsa, D. Landhuis, E. Lucero, J. McClean, X. Mi, A. Megrant, M. Mohseni, J. Mutus, M. McEwen, O. Naaman, M. Neeley, M. Niu, A. Petukhov, C. Quintana, N. Rubin, D. Sank, K. Satzinger, A. Vainsencher, T. White, Z. Yao, P. Yeh, A. Zalcman, V. Smelyanskiy, H. Neven, S. Gopalakrishnan, D. Abanin, M. Knap, J. Martinis, and P. Roushan, arXiv e-prints (2019), [arXiv:1910.06024](#).
- [31] D. Barredo, V. Lienhard, S. de Léséleuc, T. Lahaye, and A. Browaeys, *Nature* **561**, 79 (2018).
- [32] S. de Léséleuc, V. Lienhard, P. Scholl, D. Barredo, S. Weber, N. Lang, H. P. Büchler, T. Lahaye, and A. Browaeys, *Science* **365**, 775 (2019).
- [33] R. Coldea, D. A. Tennant, E. M. Wheeler, E. Wawrzynska, D. Prabhakaran, M. Telling, K. Habicht, P. Smeibidl, and K. Kiefer, *Science* **327**, 177 (2010).
- [34] C. J. Jia, E. A. Nowadnick, K. Wohlfeld, Y. F. Kung, C. C. Chen, S. Johnston, T. Tohyama, B. Moritz, and T. P. Devereaux, *Nature Comm.* **5**, 3314 (2014).
- [35] F. Liu, R. Lundgren, P. Titum, G. Pagano, J. Zhang, C. Monroe, and A. V. Gorshkov, *Phys. Rev. Lett.* **122**, 150601 (2019).
- [36] D. J. Luitz and Y. Bar Lev, *Phys. Rev. A* **99**, 010105 (2019).
- [37] K. R. Fratus and M. Srednicki, (2016), [arXiv:1611.03992](#).
- [38] P. Hauke and L. Tagliacozzo, *Phys. Rev. Lett.* **111**, 207202 (2013).
- [39] S. Sachdev, *Quantum phase transitions*, 2nd ed. (Cambridge University Press, 2011).
- [40] D. Barredo, H. Labuhn, S. Ravets, T. Lahaye, A. Browaeys, and C. S. Adams, *Phys. Rev. Lett.* **114**, 113002 (2015).
- [41] M. Knap, A. Kantian, T. Giamarchi, I. Bloch, M. D. Lukin, and E. Demler, *Phys. Rev. Lett.* **111**, 147205 (2013).
- [42] B. T. Yoshimura and J. K. Freericks, *Phys. Rev. A* **93**, 052314 (2016).
- [43] G. Pagano, A. Bapat, P. Becker, K. S. Collins, A. De, P. W. Hess, H. B. Kaplan, A. Kyprianidis, W. L. Tan, C. Baldwin, L. T. Brady, A. Deshpande, F. Liu, S. Jordan, A. V. Gorshkov, and C. Monroe, arXiv e-prints, [arXiv:1906.02700 \(2019\)](#), [arXiv:1906.02700 \[quant-ph\]](#).
- [44] M. Baiesi, C. Maes, and B. Wynants, *Phys. Rev. Lett.* **103**, 010602 (2009).
- [45] E. A. Calzetta and B.-L. B. Hu, *Nonequilibrium quantum field theory* (2008).
- [46] H. Boche and U. J. Mönich, (2019), in preparation.
- [47] J. Kempe, A. Kitaev, and O. Regev, *SIAM J. Comp.* **35**, 1070 (2004).
- [48] D. Gosset, B. Terhal, and A. Vershynina, *Phys. Rev. Lett.* **114**, 140501 (2015).
- [49] S. Lloyd and B. M. Terhal, *New J. Phys.* **18**, 023042 (2016).
- [50] A. Ciani, B. Terhal, and D. DiVincenzo, *Quant. Sc. Tech.* **4**, 035002 (2019).
- [51] Please note that while we concentrate on how these imperfections arise in those architectures, the models are relevant for all the set ups mentioned in the introduction.

- [52] O. Derzhko and T. Krokhmalksi, *Phys. Rev. B* **56**, 11659 (1997).
- [53] A. Lerose, B. Žunkovič, A. Silva, and A. Gambassi, *Phys. Rev. B* **99**, 121112 (2019).
- [54] S. N. Saadatmand, S. D. Bartlett, and I. P. McCulloch, *Phys. Rev. B* **97**, 155116 (2018).
- [55] G. M. Crosswhite, A. C. Doherty, and G. Vidal, *Phys. Rev. B* **78**, 035116 (2008).
- [56] J. Haegeman, J. I. Cirac, T. J. Osborne, I. Pižorn, H. Verschelde, and F. Verstraete, *Phys. Rev. Lett.* **107**, 070601 (2011).
- [57] M. P. Zaletel, R. S. K. Mong, C. Karrasch, J. E. Moore, and F. Pollmann, *Phys. Rev. B* **91**, 165112 (2015).
- [58] T. Hashizume, I. P. McCulloch, and J. C. Halimeh, arXiv e-prints (2018), arXiv:1811.09275.
- [59] A. S. Buyskikh, M. Fagotti, J. Schachenmayer, F. Essler, and A. J. Daley, *Phys. Rev. A* **93**, 053620 (2016).
- [60] M. B. Hastings and T. Koma, *Commun. Math. Phys.* **265**, 781 (2006).
- [61] R. Verdel, F. Liu, S. Whitsitt, A. V. Gorshkov, and M. Heyl, arXiv e-prints (2019), arXiv:1911.11382.
- [62] J. Dziarmaga, *Phys. Rev. Lett.* **95**, 245701 (2005).
- [63] W. H. Zurek, U. Dorner, and P. Zoller, *Phys. Rev. Lett.* **95**, 105701 (2005).
- [64] L. Cincio, J. Dziarmaga, M. M. Rams, and W. H. Zurek, *Phys. Rev. A* **75**, 052321 (2007).
- [65] L. Cincio, J. Dziarmaga, J. Meisner, and M. M. Rams, *Phys. Rev. B* **79**, 094421 (2009).
- [66] D. M. Kennes, C. Karrasch, and A. J. Millis, arXiv e-prints (2018), arXiv:1809.00733.
- [67] K. Kim, M. S. Chang, S. Korenblit, R. Islam, E. E. Edwards, J. K. Freericks, G. D. Lin, L. M. Duan, and C. Monroe, *Nature* **465**, 590 (2010).
- [68] E. E. Edwards, S. Korenblit, K. Kim, R. Islam, M.-S. Chang, J. K. Freericks, G.-D. Lin, L.-M. Duan, and C. Monroe, *Phys. Rev. B* **82**, 060412 (2010).
- [69] S. Schneider and G. J. Milburn, *Phys. Rev. A* **57**, 3748 (1998).
- [70] A. Friedenauer, H. Schmitz, J. T. Glueckert, D. Porras, and T. Schaetz, *Nature Phys.* **4**, 757 (2008).
- [71] From a phenomenological point of view, it is possible to estimate a threshold on the amplitude and frequency of this imperfection model to obtain a minimal change in the DSF: the oscillatory couplings are driving the system towards and away from the quantum critical point at a speed that depends on w , A , and the values of J and B . If no change is occurring in the DSF, we expect that the driving of the system has to be performed in such a way that the probability of exciting the system is low, or in other words, that the fidelity of the state evolved during the periodic driving with respect to the ground state at the given values of J and B has to be high. As mentioned in the previous section, there have been previous calculations bounding the preparation time, in the case of a linear preparation ramp, such that the excitation probability is low [63]. While these calculations are performed for linear ramps in TFIMs, the bounds derived in that work can be employed as a rough estimation of the bounds for the amplitude and frequency of the experimental driving. On one hand, we can consider that the bound needs to be calculated only for those times in which the oscillatory coupling drives the system close to the quantum critical point. On the other hand the rough estimate can be performed considering that the driving close to the quantum critical point is performed linearly, and using the bounds derived in Ref. [63] to estimate bounds on A and w . While these bounds will in no way be rigorous, they provide a good first order approximation to the experimental bounds one might need in the experimental realization of the DSF.
- [72] D. A. Abanin, J. H. Bardarson, G. De Tomasi, S. Gopalakrishnan, V. Khemani, S. A. Parameswaran, F. Pollmann, A. C. Potter, M. Serbyn, and R. Vasseur, (2019), arXiv:1911.04501.
- [73] A. Acin, I. Bloch, H. Buhrman, T. Calarco, C. Eichler, J. Eisert, D. Esteve, N. Gisin, S. J. Glaser, F. Jelezko, S. Kuhr, M. Lewenstein, M. F. Riedel, P. O. Schmidt, R. Thew, A. Wallraff, I. Walmsley, and F. K. Wilhelm, *New J. Phys.* **20**, 080201 (2018).
- [74] P. Schauss, *Quant. Sc. Tech.* **3**, 023001 (2018).
- [75] C. Schneider, D. Porras, and T. Schaetz, *Rep. Prog. Phys.* **75**, 024401 (2012).

Appendix A: Platforms considered

Rydberg atoms

For a Rydberg atoms setup, we consider the case of an array of trapped cold neutral ^{87}Rb 70S atoms with strong, controllable interactions. In this case, the atoms are trapped by optical tweezers, and the state of the art architecture can contain up to 51 atoms[24]. A two-photon process couples the ground state vector $|g\rangle = |^5\text{S}_{1/2}[\text{F} = 2, m_F = 2]\rangle$ to a target Rydberg state vector $|r\rangle = |^7\text{S}_{1/2}[m_j = 1 - 1/2]\rangle$ of the Rb atoms via an intermediate state. This transition is driven by two lasers detuned from the Rydberg state. The dynamics of the system is given by [24, 25]

$$H = \sum_i \frac{\Omega}{2} \sigma_i^x - \sum_i \Delta_i n_i + \sum_{i < j} V_{i,j} n_i n_j, \quad (\text{A1})$$

where Δ_i is a detuning factor away from the Rydberg state, Ω_i is the Rabi frequency of the atom at the i th position, $\sigma_i^x = |g_i\rangle\langle r_i| + |r_i\rangle\langle g_i|$ is the coupling between the ground state and Rydberg state, and $n_i = |r_i\rangle\langle r_i|$. The interaction strength elements $V_{i,j}$ can also be tuned by varying the distance between them or by coupling them to a different Rydberg state. To transform this Hamiltonian into an transverse field Ising model [74] we just need to identify at each site i , $|g_i\rangle = |\downarrow_i\rangle$ and $|r_i\rangle = |\uparrow_i\rangle$ such that $\sigma_i^x = (|\downarrow_i\rangle\langle\uparrow_i| + |\uparrow_i\rangle\langle\downarrow_i|)/2$ and $\sigma_i^z = (|\uparrow_i\rangle\langle\uparrow_i| - |\downarrow_i\rangle\langle\downarrow_i|)/2$, with $n_i = \mathbb{1}/2 + \sigma_i^z$. Replacing in

the Hamiltonian, we obtain a transverse field Ising model with a coupling of the form

$$H = \sum_i \frac{\Omega}{2} \sigma_i^x - \sum_i (1 - \Delta_i) n_i + \sum_{i < j} V_{i,j} \sigma_i^z \sigma_j^z. \quad (\text{A2})$$

The longitudinal field in the above expression can be suppressed by the detuning factor Δ . The Ising interaction arises from van der Waals interactions between the atoms when they are both in the Rydberg state, and takes the form $V_{i,j} = -C/r_{i,j}^6$, with $r_{i,j} = |i - j|$. As such, since the Rydberg atoms are not in the ground state once in the local trap, and the experiment is carried at a finite temperature, fluctuations in the atomic positions for each atom in each cycle of the experiment are introduced [24, 25]. This will affect the Ising interaction, Eq. (A2). We finally note that the mean lifetime of a chain scales inversely with the number of ions, with an average of 5 minutes for a chain of 53 ions.

Trapped ions

We will consider here a particular trapped ion setup, where ^{171}Yb are trapped by a linear Paul trap. A 1D spin-1/2 Ising system in the presence of a transverse field can be engineered [27] by the hyperfine "clock" states $^2S_{1/2}|F = 0, m_f = 0\rangle$ and $|F = 1, m_f = 0\rangle$ which represent the $|\downarrow_z\rangle$ and $|\uparrow_z\rangle$ eigenstates of σ_z and are separated by ν_f . These ions are trapped by a linear Paul trap, and their modes of motion are cooled near the ground state. The transverse field and spin-spin interactions can be obtained applying off-resonant laser beams [67, 68]. A transverse field can be generated by uniformly illuminating the ion chain with two Raman laser beams whose difference in frequency is tuned to the hyperfine splitting ν_f . This induces Rabi oscillations in the ions which are seen as AC Stark shifts in the spin states. On the other hand, the spin-spin interactions are created by coupling the spin states to the normal modes of motion of the ions by the Raman beams. The beams are made to carry beat note at frequencies $\nu_f \pm \mu$, which generates a spin-dependent force at frequency μ [75]. As such, controlling the beat note frequency μ , one can generate Ising interactions with a coupling given by

$$J_{i,j} = N \Omega_i \Omega_j \sum_{m=1}^N \frac{\eta_{im} \eta_{jm} \nu_m}{\mu^2 - \nu_m^2} \approx \frac{J_0}{|i - j|^\alpha}, \quad (\text{A3})$$

where Ω_i is the Rabi frequency of the i th ion, η_{im} is the Lamb-Dicke parameter of the m th mode of the i th ion at frequency ν_m , and the assumption of $|\mu - \nu_m| \gg \eta \Omega$ indicating that only virtual phonons are excited. These interactions are not necessarily uniform, since the Rabi frequency Ω_i can vary across the chain and other vibrational models can also contribute considerably. Furthermore, by tuning μ one can tune α between $0 < \alpha < 3$.

Appendix B: Numerical results for position fluctuations and random fields of Rydberg atoms

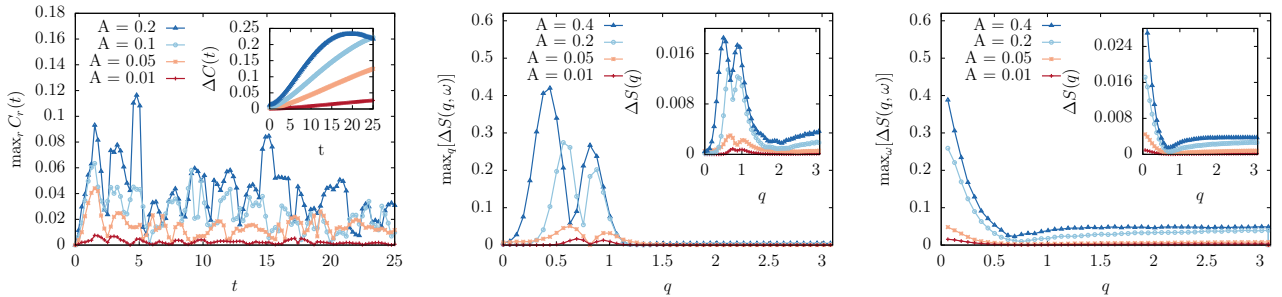


Figure 9. Error analysis of the influence of lattice imperfections on DSF for the case of random Ising interactions. (Left panel) Maximum of the absolute error for the two point correlators integrated in real space. Inset: Average absolute error of the correlators integrated over real space. (Middle panel) Maximum of the absolute error for the DSF integrated over reciprocal space. Inset: Average absolute error of the correlators integrated over reciprocal space. (Right panel) Maximum of the absolute error for the DSF integrated over frequency. Inset: Average absolute error of the correlators integrated over frequency. The DSF results show that the error is concentrated around the gap, which closes as the value of A is increased. At the same time the correlators have errors which increase in average with time, indicating that measurements at long times might be unreliable for this quantity.

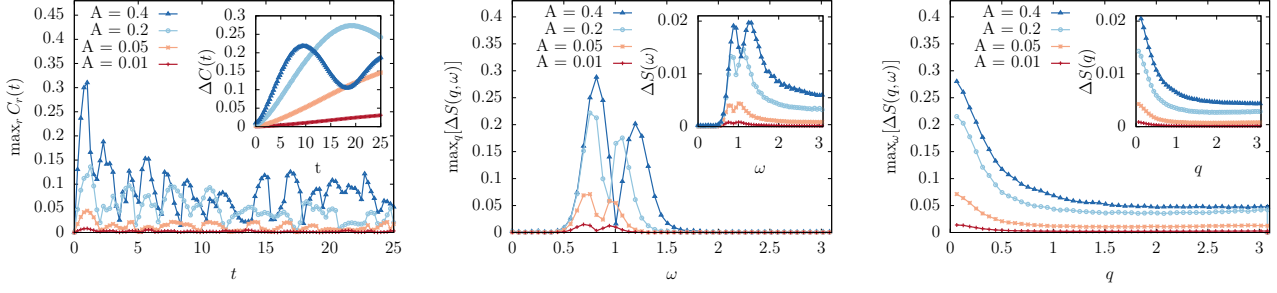


Figure 10. *Error analysis of the influence of lattice imperfections on DSF for the case of random transverse fields. (Left panel)* Maximum of the absolute error for the two point correlators integrated in real space. *Inset:* Average absolute error of the correlators integrated over real space. *(Middle panel)* Maximum of the absolute error for the DSF integrated over reciprocal space. *Inset:* Average absolute error of the correlators integrated over reciprocal space. *(Right panel)* Maximum of the absolute error for the DSF integrated over frequency. *Inset:* Average absolute error of the correlators integrated over frequency. The DSF results show that the error is concentrated around the gap, which opens as the value of A is increased. As with the previous figures, the average error increases with time, which indicates that measurements at long times might be unreliable for this quantity for this type of imperfection.

Appendix C: Dynamical structure factors for the short range transverse field Ising

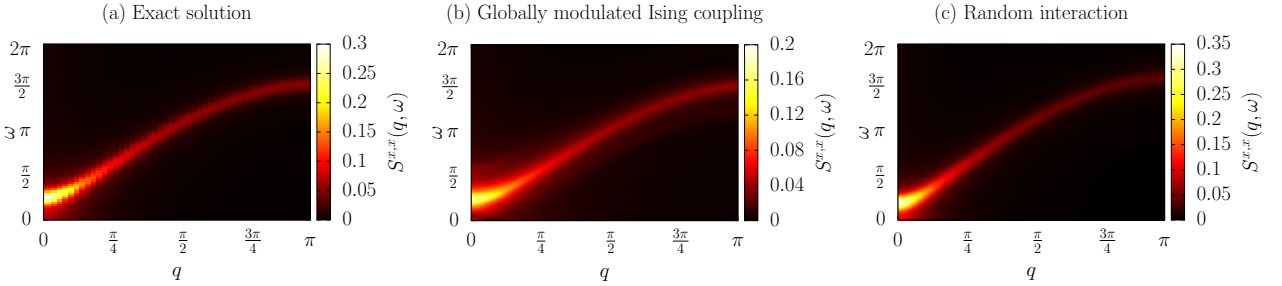


Figure 11. *DSF for the different experimental imperfections for the short range TFIM. (a)* Exact solution as obtained from our quasi-free fermionic calculation for the TFIM without imperfections, the gap is located at $q = 0$ and $\omega = \pi/4$, and we observe a clear two particle continuum for $q > 0$. *(b)* Exact solution for the case of globally fluctuating Ising couplings. In this case we observe that the shape of the low ω sector is slightly modified, but the gap and the two particle continuum can still be observed, though at a lower intensity than for (a). *(c)* Exact solution for the case of random Ising interactions. We see how the gap has closed, with the maxima located at $q = 0$ and $\omega < \pi/4$,

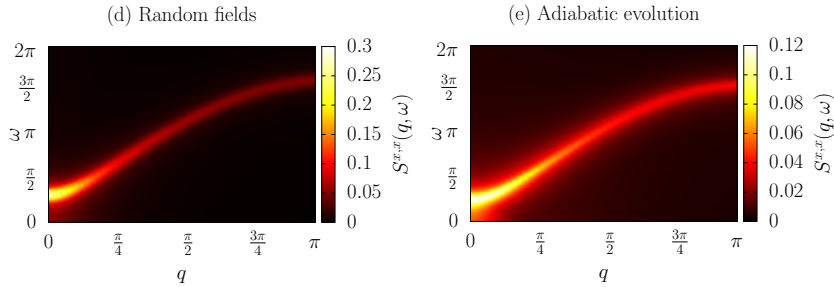


Figure 12. *DSF for the different experimental imperfections for the short range TFIM. (d)* Exact solution for the case of random transverse fields. We see how the gap has opened, with the maxima located at $q = 0$ and $\omega > \pi/4$. *(e)* Solution for case in which the ground state has been prepared by an adiabatic evolution for a time $\tau_Q = 0.5$, well below the adiabatic regime. In this case the intensity of the DSF is greatly reduced.

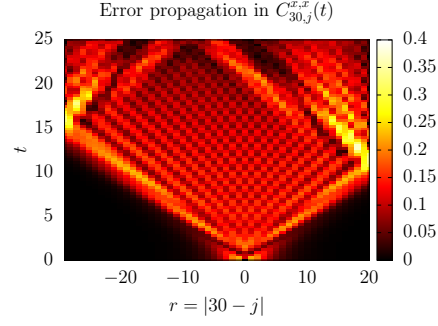


Figure 13. *Propagation of errors in the correlators.* We plot the error in the correlator with respect to a site in the middle of the chain, $C_{30,j}^{x,x}$, as a function of time. We observe the propagation of this error with a maximal velocity, creating a Lieb-Robinson cone, with an interference pattern within the cone. Indicating that errors propagate and delocalize at long times, making a direct study of many-body excitations through correlation function challenging.

Appendix D: Dynamical structure factors for the long range transverse field Ising

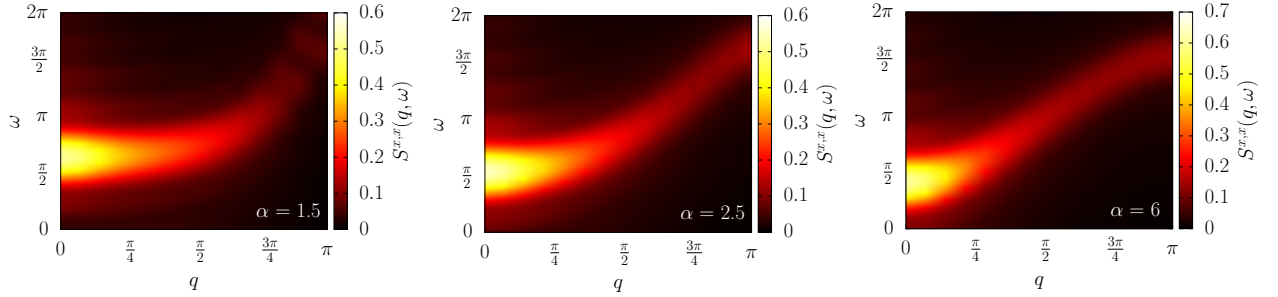


Figure 14. *DSF for the long range TFIM for the values of $\alpha = 1.5$ (left), 2.5 (middle) and 6 (right).* We see that as the value of α increases, the two particle continuum approaches the cosine form which is expected for the short range TFIM. For $\alpha < 2$ the continuum has almost no ω dependence. This can be connected to the presence of excitation confinement in this model, in which the fermionic excitations do not propagate at short times. Please note two important points. First, as recently reported, it is expected that the excitations relax at long times [61] but the time range studied in this work is not sufficiently long to see this effect. Second, unlike in previous studies [35, 53, 61], we observe the signatures of confinement in both the DSF and correlators in equilibrium, i.e., without the need of quenching the Hamiltonian.

Appendix E: Unequal time correlation function for the long range transverse field Ising

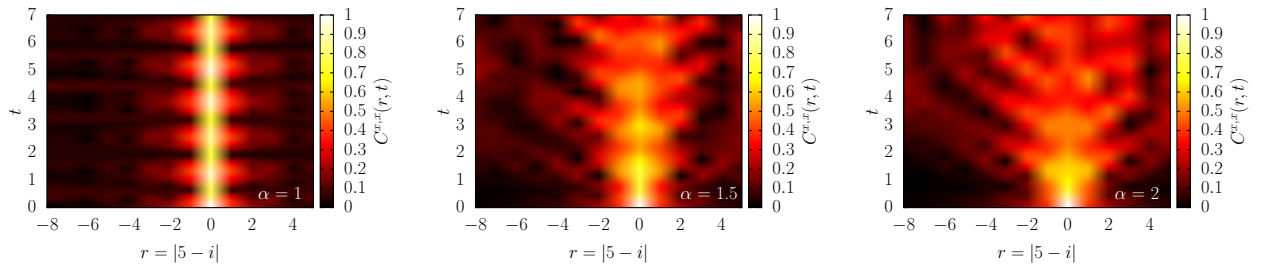


Figure 15. *Correlation function $C_{i,5}^{x,x}(t)$ for the values of $\alpha = 1$ (top), 1.5 (middle), and 2 (bottom).*

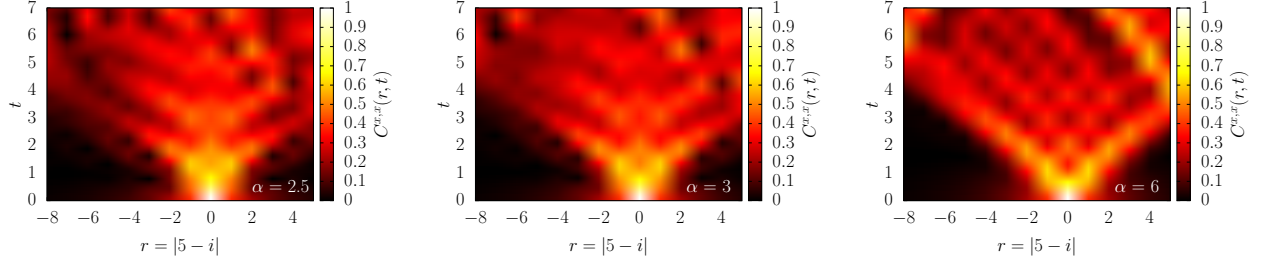


Figure 16. Correlation function $C_{i,5}^{x,x}(t)$ for the values of $\alpha = 2.5$ (top), 3 (middle), and 6 (bottom).

Appendix F: Numerical results for position fluctuations in the long range TFIM

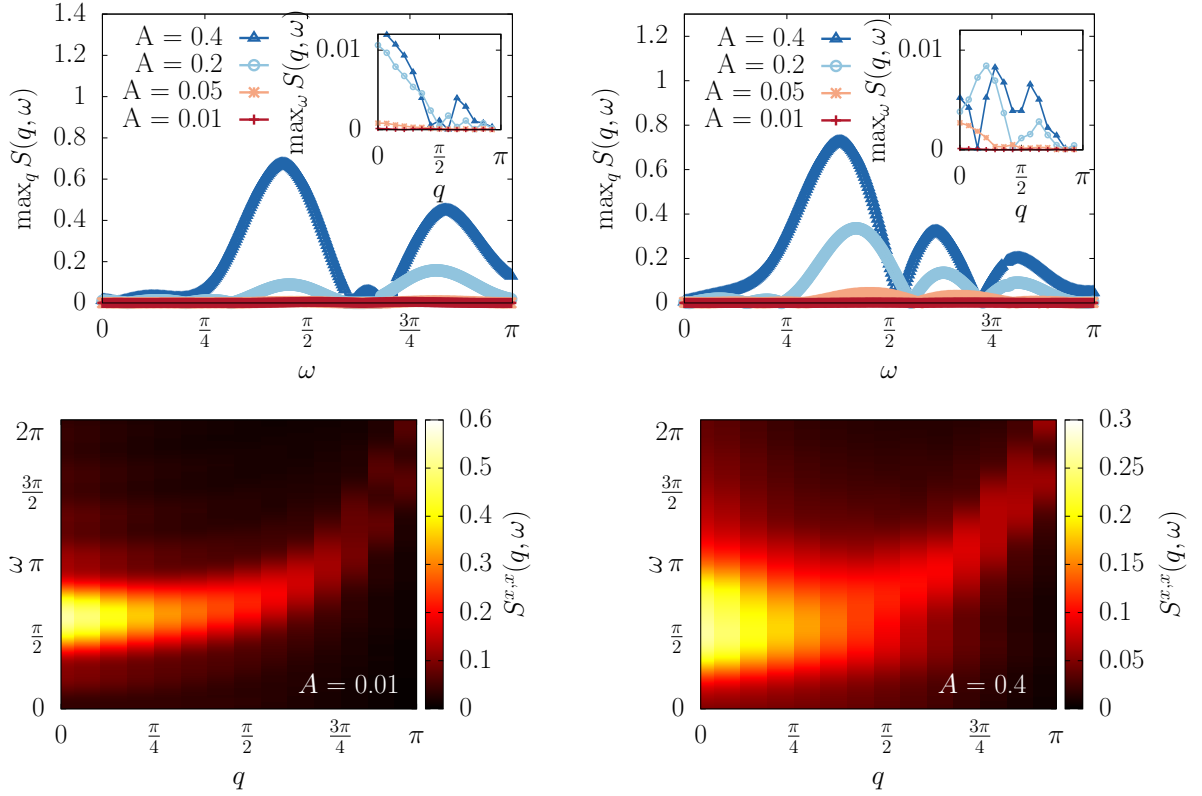


Figure 17. Numerical results for random fields in the long range TFIM. Top figures: Maximal error in the DSF for the long range TFIM with random fields, as obtained from full ED, for the cases $\alpha = 1.5$ (top left), and $\alpha = 2$ (top right). For imperfection levels within current experimental reach, $A = 0.01$ and 0.05 the error is small and well behaved on the entire $q - \omega$ domain. For imperfection levels above 0.05 the DSF is deformed, as evidenced by the maxima in the blue curves. We can compare this results to the bottom figures. Bottom figures: DSF for the long range TFIM in the presence of random fields, for the case $\alpha = 1.5$, $A = 0.01$ (bottom left) and $A = 0.4$ (bottom right). If we compare these DSFs to the clean case (left DSF in Fig. 14) we observe no discrepancies between the case $A = 0.01$ and the clean case. For the DSF corresponding to an imperfection level of 40%, $A = 0.4$ we see that the overall intensity has decreased, and the maxima has broadened considerably. The broadening of the maxima in the DSF is exhibited in the top left figure as strong and broad peaks in the maximal error as a function of frequency.